Embedding a One-column Ocean Model (SIT 1.06) in the Community Atmosphere Model 5.3 (CAM5.3; CAM5–SIT v1.0) to Improve Madden–Julian Oscillation Simulation in Boreal Winter

Yung-Yao Lan, Huang-Hsiung Hsu[*], Wan-Ling Tseng, and Li-Chiang Jiang

Research Center for Environmental Changes, Academia Sinica, Taipei 11529, Taiwan

[*]*Correspondence to*: ~~Yung-Yao Lan (yylan887@gmail.com~~Huang-Hsiung Hsu (hhhsu@gate.sinica.edu.tw)

Abstract

The effect of the air–sea interaction on the Madden–Julian Oscillation (MJO) was investigated using the one-column ocean model Snow–Ice–Thermocline (SIT 1.06) embedded in the Community Atmosphere Model 5.3 (CAM5.3; hereafter CAM5–SIT v1.0). The SIT model with 41 vertical layers was developed to simulate sea surface temperature (SST) and upper-ocean temperature variations with a high vertical resolution that resolves the cool skin and diurnal warm layer and the upper oceanic mixed layer. A series of 30-year sensitivity experiments were conducted in which various model configurations (e.g., coupled versus uncoupled, vertical resolution and depth of the SIT model, coupling domains, and absence of the diurnal cycle) were considered to evaluate the effect of air–sea coupling on MJO simulation. Most of the CAM5–SIT experiments ~~exhibited~~exhibit higher fidelity than the CAM5-alone experiment in characterizing the basic features of the MJO such as spatiotemporal variability and the eastward propagation in boreal winter. The overall MJO simulation performance of CAM5–SIT ~~benefited~~benefits from (1) better resolving the fine vertical structure of upper-ocean temperature and therefore the air–sea interaction that ~~resulted~~result in more realistic intraseasonal variability in both SST and atmospheric circulation and (2) the adequate thickness ~~and vertical resolution~~ of ~~the oceanic~~a vertically-gridded ocean mixed layer. The sensitivity experiments ~~demonstrated~~demonstrate the necessity of coupling the tropical eastern Pacific in addition to the tropical Indian Ocean and the tropical western Pacific. Coupling is more essential in the south than north of the equator in the tropical western Pacific. Enhanced MJO could be obtained without considering the diurnal cycle in coupling.

1. Introduction

The Madden–Julian Oscillation (MJO) is a tropical large-scale convection circulation system that propagates eastward across the warm pool region from the tropical Indian Ocean (IO) to the western Pacific (WP) on an intraseasonal time scale (Madden and Julian, 1972). The MJO is not just an atmospheric phenomenon. The findings ~~of the multination joint~~from a multi-nation field campaign called the Dynamics of MJO/Cooperative Indian Ocean Experiment on Intraseasonal Variability in the Year 2011~~Dynamics of the MJO (~~ (DYNAMO/CINDY2011; de Szoeke et al., 2017; Johnson and Ciesielski, 2017; Pujiana et al., 2018; Yoneyama et al., 2013; Zhang and Yoneyama, 2017) revealed vigorous air–sea coupling during the evolution of the MJO (Chang et al., 2019; DeMott et al., 2015; Jiang et al., 2015, 2020; Kim et al., 2010; Li et al., 2016; Li et al., 2020; Newman et al., 2009; Pei et al., 2018; Tseng et al., 2014). During the suppression of convection, the MJO propagates eastward with light winds, which is accompanied by enhanced downwelling shortwave radiation absorption, weaker upward latent and sensible fluxes, less cloudiness and precipitation, and weaker vertical mixing in the upper ocean, thus causing an increase in the upper-ocean temperature. In the following active phase when deep convection occurs, downwelling shortwave radiation is reduced and stronger westerly winds enhance ~~evaporation and~~ latent/sensible heat flux (LHF/SHF) loss from the ocean surface, thus causing a decrease in the upper-ocean temperature (DeMott et al., 2015; Madden and Julian, 1972, 1994; Zhang, 2005).

In addition to the ocean surface, the structure of the upper ocean also evolves. Alappattu et al. (2017) reported that during an MJO event, surface flux perturbations cause changes in the ocean thermohaline structure, thus affecting the mixed-layer temperature. The following change in sea surface temperature (SST) can further affect atmospheric circulation of the MJO. Variations in SST mediate ~~heat~~LHF and SHF

61 exchange across the air–sea interface. Although SST responds to atmospheric forcing,

62 ~~its~~the modulation of ~~surface heat fluxes~~LHF and SHF provides feedback to the

63 atmosphere (DeMott et al., 2015; Jiang et al., 2020). Li et al. (2008, 2020) proposed

64 that the phase relationship between SST and convection implies a delayed air–sea

65 interaction mechanism whereby a preceding active-phase MJO may trigger an

66 inactive-phase MJO through the delayed effect of the induced SST anomaly over the

67 IO. The reduction in SST caused by a preceding active-phase MJO may, in turn,

68 ~~yield~~yields delayed ocean feedback that initiates a suppressed-phase MJO, and vice

69 versa. The ~~nonnegligible~~by-no-means negligible effect of intraseasonal SST

70 variations caused by surface heat fluxes suggests that the ocean state can affect the

71 MJO (DeMott et al., 2015, 2019; Hong et al., 2017; Li et al., 2020).

72   Since its discovery almost five decades ago, the MJO remains a phenomenon

73 that poses a challenge to the capacity of state-of-the-art atmospheric general

74 circulation models (AGCMs) ~~and climate models~~ such as those participating in the

75 Coupled Model Intercomparison Project phase 5 and 6 to generate successful

76 simulations (Ahn et al., 2017, 2020; Bui and Maloney 2018; Jiang et al., 2020; Hung

77 et al., 2013; Kim et al., 2011).

78   Recent studies have reported that air–sea coupling improves the representation of

79 the MJO in numerical simulation (Bernie et al., 2008; Crueger et al., 2013; DeMott et

80 al., 2015; Li et al., 2016; Li et al., 2020; Tseng et al., 2014; Woolnough et al., 2007).

81 Tseng et al. (2014) indicated that effectively resolving the upper-ocean warm layer to

82 capture temperature variations in the upper few meters of the ocean could improve

83 MJO simulation. DeMott et al. (2015) suggested that the tropical atmosphere–ocean

84 interaction may sustain or amplify the pattern of the enhanced and suppressed

85 atmospheric convection of the eastward propagation. DeMott et al. (2019)

86 demonstrated that the improved MJO eastward propagation in four coupled models

87 resulted from enhanced low-level convective moistening for a rainfall rate of >5 mm

88 day^{-1} due to air–sea coupling. In addition, numerical experiments have been

89 performed to investigate the effect of the diurnal cycle on the MJO (Hagos et al.,

90 2016; Oh et al., 2013), with the results suggesting that the strength and propagation of

91 the MJO through the Maritime Continent (MC) were enhanced when the diurnal cycle

92 was ignored.

93   Although previous studies have demonstrated the importance of considering the

94 air–sea interaction in a numerical model to improve MJO simulation, additional

95 details regarding model configuration (e.g., vertical resolution, and depth of the ocean

96 mixed layer, coupling domain, and absence of the diurnal cycle in air-sea coupling)

97 have not been systematically explored. Tseng et al. (2014) coupled the one-column

98 ocean model Snow–Ice–Thermocline (SIT; Tu and Tsuang, 2005) to the fifth

99 generation of the ECHAM AGCM (ECHAM5–SIT) and indicated that a vertical

100 resolution of 1 m was essential to yield an improved simulation of the MJO with a

101 realistic strength and eastward propagation speed.

102   In this study, we coupled the SIT model to the Community Atmosphere Model

103 version 5.3 (CAM5.3; Neale et al., 2012)—the atmosphere component of the

104 Community Earth System Model version 1.2.2 (CESM1.2.2; Hurrell et al., 2013)—to

105 explore how the air–sea interaction in AGCMs can improveimprovement of MJO

106 simulation by coupling SIT model to another AGCM is reproducible in modeling

107 science. The CAM5.3, which has been widely used for the long-term simulation of the

108 climate system, could not efficiently simulate the eastward propagation of the MJO;

109 instead, the model simulated a tendency for the MJO to move westward in the IO

110 (Boyle et al., 2015, Jiang et al, 2015). By contrast, the updated CESM2 with the new

111 CAM6 could realistically simulate the MJO (Ahn et al., 2020; Danabasoglu et

112 al., 2020). Thus, the well-explored CAM5, which does not produce a realistic MJO,

113   appears to be a favorable choice for exploring ~~how~~ coupling a simple one-dimensional

114   (1-D) ocean model, such as the SIT model, can improve MJO simulation, as well as

115   the effects of model configuration~~.~~ on the degree of the improvement. Such a study

116   can also enhance our understanding regarding the effect of air–sea coupling~~'s effect~~

117   on the MJO.

118   ~~This study examined how air–sea coupling can improve MJO simulation,~~

119   ~~especially that of the eastward propagation that has been poorly simulated in many~~

120   ~~climate models.~~ The MJO that exhibits a more substantial eastward propagation in

121   boreal winter than in other seasons was the targeted feature in this study. ~~We~~To

122   examine the sensitivity of MJO simulations to different configurations of air-sea

123   coupling, we conducted a series of 30-year numerical experiments by considering

124   various model configurations (e.g., coupled versus uncoupled, vertical resolution and

125   depth of the SIT model, coupling domains, and absence of the diurnal cycle) to

126   investigate the effect of air–sea coupling. This paper is organized as follows. Section

127   2 describes the data~~, methodology~~ for validation, the model used for simulation, and

128   ~~model setup. Section 3 presents the~~ the design of ~~coupled model~~numerical

129   experiments. Section 4~~3~~ describes the effect of various ~~model~~air-sea coupling

130   configurations on the MJO simulation determined through detailed MJO diagnostics.

131   ~~A discussion~~Discussion and conclusions are provided in Section 5~~4~~.

132

133   **~~2.~~ 2. Data, methodology, ~~and~~ model description, and experimental designs**

134   **~~2.1 Observational data and analysis methods~~**

135   **2.1 Data and methodology**

136   The data analyzed in this study include precipitation from the Global

137   Precipitation Climatology Project~~,~~ (GPCP), outgoing longwave radiation (OLR) and

138   daily SST (Optimum Interpolation SST; OISST) from the National Oceanic and

139 Atmosphere Administration (NOAA), and parameters from the ERA-Interim (ERA-I)

140 reanalysis (Adler et al., 2003; Dee et al., 2011; Lee et al., 2011; Reynolds and Smith,

141 1995; Schreck et al., 2018). The ~~initial~~ SST data for the SIT model were obtained

142 from the Hadley Centre Sea Ice and Sea Surface Temperature dataset (Rayner et al.,

143 2003; HadISST1) and the ocean subsurface data (40-layer climatological ocean

144 temperature, salinity, and currents) for nudging were retrieved from the National

145 Centers for Environmental Prediction (NCEP) Global Ocean Data Assimilation

146 System (GODAS; Behringer and Xue, 2004). ~~Ocean bathymetry was derived from the~~

147 ~~NOAA ETOPO1 data (Amante and Eakins, 2009) and interpolated into 1.9° × 2.5°~~

148 ~~horizontal resolution.~~

149   We used the CLIVAR MJO Working Group diagnostics package (CLIVAR,

150 2009) and a 20–100-day filter (Kaylor, 1977; Wang et al., 2014) to determine

151 intraseasonal variability. MJO phases were defined following the index (namely,

152 RMM1 and RMM2) proposed by Wheeler and Hendon (2004), which considers the

153 first two principal components of the combined near-equatorial OLR and zonal winds

154 at 850 and 200 hPa. The band-passed filtered data were used for calculating the index

155 and defining phases.

156

157 **2.2 Model description**

158 **2.2.1 CAM5.3**

159   The CAM5.3 used in this study has a horizontal resolution of 1.9° latitude ×

160 2.5° longitude and 30 vertical levels with the model top at 0.1 hPa. The MJO could

161 not be realistically simulated in the CAM5.3. Boyle et al. (2015) demonstrated that

162 although making the deep convection dependent on SST improved the simulation of

163 the MJO variance, it exerted a significant negative effect on the mean-state climate of

164 low-level cloud and absorbed shortwave radiation. By comparing the simulation

165 results of an uncoupled and coupled CAM5.3, Li et al. (2016) suggested that air–sea

166 coupling and the convection scheme most significantly affected the MJO simulation

167 in the climate model.

168

169 **2.2.2 1-D high-resolution TKE ocean model**

170   The 1-D high-resolution turbulence kinetic energy (TKE) ocean model SIT was

171 used to simulate the diurnal fluctuation of SST and surface energy fluxes. (Lan et

172 al., 2010; Tseng et al., 2014; Tu and Tsuang, 2005). The model was well verified

173 against ~~surface and subsurface observations in~~in situ measurements on board the R/V

174 Oceanographic Research Vessel 1 and 3 over the South China Sea (Lan et al., 2010)

175 and on R/V Vickers over the tropical WP (Tu and Tsuang, 2005). ~~Variations in sea~~

176 ~~water temperature (T), current ($\vec{u}$), and salinity (S) were determined (Gaspar et al.,~~

177 ~~1990) using the following equations.~~

178 $$\frac{\partial T}{\partial t} = (k_h + v_h)\frac{\partial^2 T}{\partial z^2} + \frac{R_{sn}}{\rho_{w0}c_w}\frac{\partial F}{\partial z} \hspace{3cm} (1)$$

179 $$\frac{\partial \vec{u}}{\partial t} = -f\ \hat{k} \times\ \vec{u} + (k_m + v_m)\frac{\partial^2 \vec{u}}{\partial z^2} \hspace{3cm} (2)$$

180 $$\frac{\partial S}{\partial t} = (k_h + v_h)\frac{\partial^2 S}{\partial z^2} \hspace{4cm} (3)$$

181 ~~where R_{sn} is the net solar radiation at the surface (W m^{-2}), $F(z)$ is the fraction~~

182 ~~(dimensionless) of R_{sn} that penetrates to the depth z, and k_h and k_m are eddy diffusion~~

183 ~~coefficients for heat and momentum (m^2 s^{-1}), respectively. The value of k_h within the~~

184 ~~cool skin layer and that of k_m within the viscous layer were set to zero. Molecular~~

185 ~~transport is the only mechanism for the vertical diffusion of heat and momentum in~~

186 ~~the cool skin and viscous layer, respectively (Hasse, 1971; Grassl, 1976; Wu,~~

187 ~~1985).The parameters v_m and v_h are the molecular diffusion coefficients for~~

188 ~~momentum and temperature, respectively, ρ_{w0} is the density (kg m^{-3}) of water, and~~

189 ~~c_w is the specific heat capacity at constant pressure (J kg^{-1} K^{-1}). S is salinity (‰), $\vec{u}$~~

190 is the current velocity (m s^{-1}), f is the Coriolis parameter (dimensionless), and $\hat{k}$ is

191 the vertical unit vector (m s^{-1}).

192   The eddy diffusivity for momentum k_m is simulated using an eddy kinetic energy

193 approach based on the Prandtl–Kolmogorov hypothesis as follows:

$$k_m = c_k l_k \sqrt{E} \tag{3}$$

195 where $c_k = 0.1$ (Gaspar et al., 1990), l_k is the mixing length (m), and

196 $E = 0.5\left(u'^2 + v'^2 + w'^2\right)$ is turbulent kinetic energy. The turbulent kinetic energy (E)

197 is determined using a 1-D equation (Mellor and Yamada, 1982) as follows:

$$\frac{\partial E}{\partial t} = \frac{\partial}{\partial z} k_m \frac{\partial E}{\partial z} + k_m \left(\frac{\partial \bar{u}}{\partial z}\right)^2 + k_h \frac{g}{\rho_w} \frac{\partial \rho_w}{\partial z} - c_\varepsilon \frac{E^{3/2}}{l_\varepsilon} \tag{4}$$

199 where $c_\varepsilon = 0.7$ (Gaspar et al., 1990), g is the gravity (m s^{-2}), ρ_w is the density of

200 water (kg m^{-3}), and l_ε is the characteristic dissipation length (m). The mixing length

201 (l_k) and dissipation length (l_ε) were determined following the approach reported by

202 Gaspar et al. (1990). This approach is valid for determining the eddy diffusivity of

203 both the ocean mixed layer and surface layer.

204   In the SIT model setting, the specific heat of sea water is a constant (4186.84 J

205 kg^{-1} K^{-1}), and the Prandtl number in water is defined as the ratio of momentum

206 diffusivity to thermal diffusivity, which is a dimensionless number set as a constant

207 (1.0). The kinematic viscosity is a constant (1.14 × 10^{-6} m^2 s^{-1}; Paulson and

208 Simpson, 1981), and the downward solar radiative flux into water with nine

209 wavelength bands was determined following the approach reported by Paulson and

210 Simpson (1981). The minimum turbulent kinetic energy is set to 10^{-6} m^2 s^{-2}, and the

211 zero displacement is set to 0.03 m.

212   The SIT model determines the vertical profiles of the temperature and

213 momentum of a water column from the surface down to the seabed~~.~~, except in the

214 fixed ocean model bottom experiment. The default setting of vertical discretization

215 (e.g., in the control coupled experiment) is 41 layers with 12 layers in the first 10.5 m,

216 6 layers between 10.5 m and 107.8 m (Supplementary Information I). In the 1-D TKE

217 ocean model, temperature and salinity below 107.8 m, where vertical mixing is

218 greatly weakened, are nudged toward the climatological values of GODAS data until

219 4607 m. The extra high vertical resolution is needed to catch detailed temporal

220 variation of upper ocean temperature characterized by the warm layer and cool skin

221 (Tu and Tsuang, 2005). To account for the neglected horizontal advection heat flux,

222 the ocean is weakly nudged (by using a 30-day time scale) between 10.5 m and

223 ~~100~~107.8 m and strongly nudged (by using a 1-day time scale) below ~~100~~107.8 m

224 according to the NCEP GODAS climatological ocean temperature~~; no~~. No nudging is

225 performed ~~for depths under 10 m. Considerably fine 41-layer vertical discretization is~~

226 ~~applied, with 12 layers in~~within the upper~~-~~most 10.5 m. ~~The resolution in the upper 10~~

227 ~~m is considerably fine to capture the upper-ocean warm layer, and the thickness of the~~

228 ~~first layer below sea surface is 0.05 mm to reproduce the ocean surface cool skin. The~~

229 ~~41 levels are at the surface and at the depths of 0.05 mm, 1.0 cm, 2.0 cm, 3.0 cm, 4.0~~

230 ~~cm, 5.0 cm, 6.0 cm, 7.0 cm, 8.0 cm, 9.0 cm, 10.0 cm, 16.8 cm, 29.5 cm, 43.6 cm, 59.2~~

231 ~~cm, 76.9 cm, 96.8 m, 119.4 cm, 145.3 cm, 174.9 cm, 208.9 m, 248.3 cm, 293.8 cm,~~

232 ~~346.8 cm, 408.4 cm, 480.2 cm, 564.3 cm, 662.6 cm, 777.9 cm, 913.1 cm, 1072.0 cm,~~

233 ~~1258.8 cm, 1478.6 cm, 1737.3 cm, 2042.0 cm, 2401.1 cm, 2824.4 cm, 3323.6 cm,~~

234 ~~3912.4 cm, and 4607.1 cm.~~ The SIT model calculates ~~data two times~~twice for each

235 CAM5 time step (30 min; i.e., coupling 48 times per day).

236

237 **2.3~~.~~ Experimental ~~setup~~design**

238 ~~Five sets~~A series of 30-year numerical experiments (Table 1) were conducted to

239 investigate the effect of the air–sea interaction on the MJO simulation. ~~In all simulations,~~The HadSST1 used to force the ~~CAM5.3~~ coupled and uncoupled model

240

241 was ~~forced by observed~~ the climatological monthly ~~SST except~~ mean SST averaged

242 over 1982-2001. The monthly SST was linearly interpolated to daily SST fluctuation

243 that forced the model. The SST in ~~the~~air–sea coupling region ~~where the SIT model~~

244 ~~determined the upper ocean temperature. The~~ was recalculated by the SIT during the

245 simulation, while the prescribed annual cycle of SST was used in the areas outside the

246 coupling region. Ocean bathymetry of the SIT was derived from the NOAA ETOPO1

247 data (Amante and Eakins, 2009) and interpolated into 1.9° × 2.5° horizontal

248 resolution.

249 All simulations were driven by the prescribed annual cycle of SST repeatedly for

250 30 years. The strategy is to evaluate the simulation capacity of climate models under

251 the same condition without considering interannual variation induced by SST. This

252 approach has been widely adopted in many studies (Delworth et al., 2006; Haertel et

253 al., 2020; Subramanian et al., 2011; Tseng et al., 2014; Wang et al., 2005).

254 Atmospheric initial conditions and external forcing such as CO_2, ozone, and

255 aerosol in near-equilibrium climate state around the year 2000 were taken from

256 F_2000_CAM5 component set based on CESM1.2.2 framework development. The

257 data has been commonly used in present-day simulations using CAM5 (e.g., He et al.,

258 2017).

259 The setup of five sets of experiment ~~sets were~~ conducted in this study are

260 described as follows.

261 (1) ~~a~~A standalone CAM5.3 simulation forced by ~~observed~~ climatological monthly

262 ~~SST~~HadISST1 (A–CTL) and ~~a~~the control experiment of coupled CAM5–SIT–

263 ~~v1.0~~ simulation (C–30NS; 41 vertical levels, coupling in the entire tropics

264 between 30°~~S~~N and 30°~~N~~S with a diurnal cycle~~);~~).

(2) ~~an upper~~Upper-ocean vertical resolution experiment ~~(C LR12m and C LR34m):~~ ~~two coarse vertical resolution simulations with a thickness of 11.8 and 34.2 m,~~ ~~respectively, at the third layer; (3) a lower ocean boundary experiment~~: ~~three~~Two simulations with the ~~lower boundary of the SIT model~~first layer centering at 12 m (C–LR12m) and 34 m (C–LR34m). Further details of the experimental design are shown in supplementary Fig. S1.

(3) Shallow ocean bottom experiment: Three simulations with the ocean model bottom at 10 m (C–HR1mB10m), 30 m (C–HR1mB30m), and 60 m (C–HR1mB60m~~];~~) (supplementary Fig. S2).

(4) ~~a regional~~Regional coupling experiment: Four simulations with ~~four~~the coupling ~~domains, namely the latitudinal effect [~~region in 0°N–30°N (C–0_30N) and 0°S–30°S (C–0_30S~~] and the longitudinal~~) for latitudinal effect ~~[, and ~~30°E–180°E (C–30_180E) and 30°E–75°W (C–30E_75W~~) (see the~~) for longitudinal effect. The coupling ~~domain~~domains are shown in Fig. 1~~); and~~.

(5) ~~a ~~A non-diurnal ~~coupling experiment: a nondiurnal ~~simulation (C–30NS–nD) that considers the air–sea interaction ~~by ~~only once a day, namely, calculating ~~ocean surface fluxes ~~SHF and LHF based on daily mean atmospheric variables and SST ~~(C 30NS nD), with~~. To prevent the inconsistent local time in different regions, the coupling frequency ~~maintained~~at each grid point remained 48 times per day ~~to prevent the local time in different regions from being inconsistent when coupling once a day. Greenhouse gas concentrations were fixed at the ~~using the same daily means of atmospheric variables and SST at that particular point. In contrast, the control simulation calculates air-sea fluxes 48 times a day based on instantons values ~~observed in the year 2000~~. A comparison between the non-diurnal simulation and the control simulation reveals the effect of diurnal cycle in air0sea coupling.

291 ~~The main codes of the SIT model in Fortran 90 are packaging in independent~~
292 ~~and original subprograms, with data and interface blocks in modules, that creates~~
293 ~~explicit interfaces between the CAM5.3 and the SIT model without a coupler. In~~
294 ~~addition, these modules contain dynamically allocable arrays and the independent I/O~~
295 ~~procedures of the SIT model. The coupler in the CAM5–SIT only brokers~~
296 ~~communication interchanges between the simulated SST and calculated oceanic~~
297 ~~surface fluxes.~~

298

299   4

3. Results and Discussion

301   The realistic simulation of the MJO has always been a major bottleneck in the
302 development of climate models. In this section, we demonstrate ~~how~~the sensitivity of
303 air–sea coupling experiments using a 1-D high-resolution ocean ~~mixed-layer~~ model
304 significantly improves the MJO simulation by the CAM5.3. The period between
305 November and April when the MJO is the most prominent was the targeted season in
306 this study.

307

4 3.1 Improvement of MJO simulation through air–sea coupling

309   This subsection compares the MJO simulation of the control coupled
310 ~~model~~experiment (C–30NS) with that of the uncoupled AGCM (A–CTL) forced by
311 climatological monthly SST of HadISST1 to demonstrate the effect of air–sea
312 coupling on the MJO simulation by coupling the SIT model to the CAM5.3 in the
313 tropical belt (30°N–30°S).

314

4 3.1.1 Wavenumber–frequency spectra and eastward propagation characteristics

316   A wavenumber–frequency spectrum (W–FS) analysis was conducted to quantify

317 propagation characteristics simulated in different experiments. The spectra

318 of unfiltered U850 in ~~observation~~ERA-I reanalysis, C–30NS, and A–CTL are shown

319 in Fig. 2a–c, respectively. The ~~coupled~~ C–30NS ~~effectively simulated~~considering the

320 ~~observed~~coupling in 30ºN–30ºS realistically simulates eastward-propagating signals

321 at zonal wavenumber 1 and 30–80-day periods (Fig. 2a–b), although with a slightly

322 larger amplitude~~.~~ compared with ERA-I. By contrast, the uncoupled A–CTL ~~did~~does

323 not ~~effectively simulate the observed characteristics~~yield realistic simulation; instead,

324 it ~~simulated~~simulates both eastward (wavenumber 1)- and westward (wavenumber 2)-

325 propagating signals with an unrealistic spectral shift to time scales longer than ~~the~~

326 ~~observed~~ 30–80-day ~~period~~.

327   The major features of the simulated MJO propagation were examined. Figure

328 2d–f show the time evolution of ~~intraseasonal~~ precipitation and U850 anomalies in

329 Hovmöller diagrams~~; specifically,~~, which represent lagged correlation coefficients

330 between the precipitation ~~at~~averaged over 10°S–5°N, 75–100°E ~~with~~and the ~~average~~

331 precipitation ~~at~~and U850 averaged over 10°N–10°S ~~and U850 anomalies along the~~

332 ~~equator~~on intraseasonal timescales. Figure 2d indicates eastward propagation for both

333 precipitation and U850 from the eastern IO to the dateline, with precipitation leading

334 U850 by approximately a quarter of a cycle. The Hovmöller diagram derived from the

335 C–30NS (Fig. 2e) exhibits the key characteristics of eastward propagation for both

336 precipitation and U850 and the relative phases between the two, although the

337 simulated correlation ~~was~~is slightly weaker than that ~~observed.~~derived from GPCP

338 and ERA-I. By contrast, the uncoupled A–CTL ~~simulated~~simulates intraseasonal

339 signals that ~~propagated~~propagate westward over the IO and ~~simulated~~ weak and much

340 slower eastward propagation crossing the MC and WP (Fig. 2f). The contrast between

341 Fig. 2e and 2f ~~demonstrated~~demonstrate that coupling a 1-D ~~ocean~~ TKE ocean model

342 alone could lead to a significant improvement in an AGCM in simulating the major

343 characteristics (e.g., amplitude, propagation direction and speed, and phase

344 relationship between precipitation and circulation) of the MJO.

345

346 **~~4~~3.1.2 Coherence of the simulated MJO**

347   Cross-spectral analysis was ~~performed~~conducted to examine the coherence and

348 phase lag between tropical circulation and convection, which were plotted over the

349 tropical wave spectra. Figure 2g–i show the symmetric part (e.g., Wheeler and

350 Kiladis, 1999) of OLR and U850 in ~~observation~~ERA-I/NOAA data, C–30NS, and A–

351 CTL, respectively. We present only ~~a magnified display of~~ the spectra between ~~the~~

352 ~~frequency of~~ 0 to 0.35 day^{-1} to highlight the MJO and equatorial Kelvin waves. The

353 most prominent ~~characteristic observed was~~characteristics seen in ERA-I/NOAA data

354 are the peak coherence at wavenumbers 1–3 and a phase lag of approximately 90° in

355 the 30–80-day band ~~for the symmetric component associated with the MJO~~ (Ren et

356 al., 2019; Wheeler and Kiladis 1999). The coupled experiment C–30NS

357 ~~simulated~~simulates strong coherence in this low-frequency band (wavenumber 1) and

358 ~~exhibited~~exhibits a realistic phase lag relationship between U850 and OLR

359 perturbations. However, the coherence at wavenumbers 2–3 for the 30–80-day period

360 simulated by C–30NS ~~was~~is weaker than that ~~observed. In addition, this~~in ERA-

361 I/NOAA data. This undersimulation was also noted in CCSM4 (Subramanian et al.,

362 2011), the uncoupled and coupled CAM4 and CAM5 (Li et al., 2016), and NorESM1-

363 M (Bentsen et al., 2013), which had a version of the CAM as an AGCM. In summary,

364 C–30NS ~~produced~~considering the coupling between 30ºN–30ºS produces coherent

365 and energetic patterns in the eastward-propagating intraseasonal fluctuations of U850

366 and OLR in the tropical IO and WP that are generally consistent with the MJO

367 characteristics. By contrast, the MJO characteristics in A–CTL ~~were~~are considerably

368 weaker than those in C–30NS and that ~~observed~~in ERA-I/NOAA data.

369

43.1.3 Horizontal and vertical structures of the MJO across the MC

Figure 2j–o show the horizontal and vertical structures of the MJO when deep

convection is the strongest over the MC (i.e., phase 5). Figure 2j–l present the 20–

100-day filtered OLR (W m^{-2}, shaded) and 850-hPa wind (m s^{-1}, vector). C–30NS

realistically simulated the enhanced tropical convection over the eastern IO and the

Kelvin-wave-like easterly anomalies over the tropical WP despite undersimulating

the convection over the MC (Fig. 2j and 2k). By contrast, A–CTL failed to simulate

the enhanced convection over the eastern IO and MC; instead, it simulated

considerably weaker convection and easterly winds over the MC and WP,

respectively, than that ~~observed~~in ERA-I/NOAA data (Fig. 2j and 2l).

Figure 2m–o show the vertical–longitudinal profiles of 20–100-day filtered

15°N–15°S averaged vertical velocity (OMEGA; Pa s^{-1}, shaded) and moist static

energy (MSE) anomalies (W m^{-2}, contour) at phase 5. The spatial distribution of

negative OMEGA (ascending motion) anomalies generally agreed with OLR

anomalies in C–30NS simulation and ~~observation~~NOAA data over the Indo-Pacific

region (Fig. 2m and 2n). The ~~observed relative~~relatively spatial relationship between

the ascending motion and MSE ~~was~~seen in ERA-I is well simulated in the coupled

experiment C–30NS. For example, positive MSE anomalies on the eastern side of the

anomalous ascent ~~demonstrated~~demonstrate that the energy recharge process occurs in

advance of the MJO convection over the lower-tropospheric easterlies (Fig. ~~2j~~2m and

~~2k~~2n), whereas negative MSE anomalies on the western side ~~revealed~~reveal that the

discharge process occurs during and after convection over the lower-tropospheric

westerlies. By contrast, this phase relationship, considered to be an essential feature

leading to the eastward propagation of an MJO (Hannah and Maloney 2014; Heath et

al., 2021), ~~was~~is not properly simulated in the uncoupled experiment A–CTL (Fig.

395 2o), in which the simulated weak negative OMEGA ~~was~~is located between negative

396 and positive MSE anomalies over weak lower-tropospheric wind anomalies and

397 associated with weak convection over the MC (Fig. 2l).

398   The ~~observed~~ temporal evolution of NOAA OLR and ERA-I U850 (Fig. 3a)

399 ~~indicated~~indicates that convection originating in the western IO ~~was~~is enhanced

400 during its eastward propagation to the MC where it ~~reached~~reaches the peak

401 amplitude and then gradually weakened when continuing moving eastward to the

402 dateline. ~~In~~In the coupled experiment C–30NS, this evolution of convectively

403 coupled circulation ~~was~~is realistically simulated, although it ~~was~~is weaker than the

404 ~~observed~~ strength seen in NOAA OLR (Fig. 3b). Moreover, the split of convection

405 into two cells off the equator in phase 6 ~~was~~is appropriately simulated in C–30NS

406 (P6 in Fig. 3a and 3b). This split was caused by the topographic and land–sea

407 contrast effects of the MC (Tseng et al., 2017). Associated with the split ~~was~~is the

408 southward detouring of the anomalous convection during the passage of the MJO

409 through the MC (Kim et al. 2017, Tseng et al., 2017; Wu and Hsu, 2009). After the

410 passage of the MJO through the MC, the anomalous convection ~~stayed~~stays south of

411 the equator and ~~continued~~continues moving eastward to the dateline. In the

412 uncoupled A–CTL, the systematic eastward propagation of convectively coupled MJO

413 circulation from the IO into the MC ~~was~~is not simulated. Instead, the convection over

414 the MC ~~developed~~develops in situ at a later stage than that observed (e.g., P6 in Fig.

415 3c) and dissipated rapidly. The A–CTL ~~simulated~~simulates a pair of off-equator

416 convection anomalies in the eastern IO during phase 2 (P2 in Fig. 3c) that

417 ~~moved~~moves westward toward the central IO and were amplified at later stages (e.g.,

418 P4 in Fig. 3c). This unrealistic evolution explains the westward propagation tendency

419 observed in the Hovmöller diagram (Fig. 2f).

420

4~~3~~.1.4 Characteristics of air–sea interaction

Figure 4a–c show the longitude–phase diagram in which the 20–100-day filtered precipitation (shaded) and SST (contour) anomalies were averaged over 10°S–10°N to determine the relationship between precipitation and SST fluctuations and to establish a link between air–sea coupling and convection. The propagation of the enhanced convection with positive SST anomalies to the east could be clearly seen in ~~observation~~GPCP/OISST and ~~the coupled experiment~~ C–30NS (Fig. 4a and 4b). The highest SST anomaly (SSTA) ~~led~~leads the maximum precipitation anomaly by approximately 2–3 phases, and the SSTA ~~began~~begins to decrease following the onset of enhanced precipitation. The ~~observation revealed~~ERA-I and OISST data reveal the following relationship between net surface flux and SST: the decreased (increased) ~~latent/sensible heat fluxes~~LHF/SHF and increased (decreased) downward radiation flux leading (lagging) the positive (negative) SSTA east (west) of anomalous deep convection. This well-known lead–lag relationship reflecting the active air–sea interaction in an MJO ~~was~~is realistically simulated in the coupled experiment C–30NS (not shown).

The contrast between C–30NS and A–CTL confirms the key role of the air–sea interaction in contributing to the eastward propagation and demonstrates that the eastward propagation simulation can be markedly improved by incorporating the air–sea interaction process in the model, even when using a simple 1-D ocean model such as SIT.

4~~3~~.1.5 Vertically tilting structure

The warm SST was the key forcing that contributed to the boundary layer convergence before the onset of deep convection (Li et al., 2020; Tseng et al., 2014). Hence, the warmer upper ocean enhances the low-level atmospheric convergence and

447 then leads to enhanced low-level moisture and preconditioned deep convection and

448 eastward propagation. This moistening process associated with warm ocean surface

449 temperature ~~was~~is well simulated in the coupled experiment C–30NS but is not shown

450 here. Instead, we present the coupling of moisture divergence (MD) and atmospheric

451 circulation.

452   MD and zonal wind anomalies from the surface to the upper troposphere

453 averaged over the 10°S–10°N and 120–150°E region are shown in Fig. 4d–f to depict

454 the relationship between the vertically tilting structure of MD and zonal wind

455 anomalies. Note that the active convection occurred around phase 5. The coupled

456 experiment C–30NS (Fig. 4e) realistically ~~simulated~~simulates the ~~observed~~

457 deepening of coupled MD and zonal wind anomalies with time (Fig. 4d). An

458 evolution from the right to left seen in each panel of Fig. 4d–f ~~was~~is equivalent to

459 the eastward movement of vertically tilting circulation from the eastern IO into the

460 MC because of the eastward-propagating nature of the MJO. Figure 4d and 4e show

461 that in both ~~observation and~~ERA-I reanalysis and the coupled experiment C–30NS,

462 the near-surface convergence (negative MD) occurring in the easterly anomalies

463 ~~led~~lead the convection and continued deepening up to 500 hPa from phase 2 to

464 phase 6 when the easterly anomalies ~~switched~~switch to westerly anomalies. By

465 contrast, this ~~observed~~ evolution of coupled MD–zonal wind anomalies ~~were~~are not

466 appropriately simulated in the uncoupled experiment (Fig. 4f). For example, a slow

467 deepening with time ~~was~~is observed in the MD anomaly but not in the zonal wind

468 anomaly that ~~exhibited~~exhibits a vertically decayed structure, suggesting that MD

469 and wind anomalies ~~were~~are not well coupled, as noted in ~~observation~~the ERA-

470 I/NOAA data and the control coupled experiment.

471 In ~~observation~~the ERA-I reanalysis data, the negative near-surface MD

472 anomalies ~~appeared~~appear first under the easterly anomaly and ~~continued~~continue

473   deepening between the easterly and westerly anomalies. This development in the

474   phase relationship between MD and zonal wind anomalies in both observationERA-

475   I reanalysis data and the coupled simulation is consistent with the well-known

476   structure embedded in the MJO, namely the near-surface convergence in the easterly

477   phase (i.e., a boundary-layer moistening process; Kiranmayi and Maloney 2011; Li

478   et al., 2020; Tseng et al., 2014), followed by the deep convection when transitioning

479   to the westerly phase. This close phase relationship that is key to the eastward

480   propagation wasis appropriately simulated in the coupled experiment but not in the

481   uncoupled experiment.

482

483   **43.1.6 Intraseasonal variance of precipitation**

484   Figure 4g–i present the spatial distribution of intraseasonal variance of

485   precipitation. In observationthe GPCP data, the maximum variance wasis noted over

486   the tropical eastern IO, MC, and tropical WP. The maximum variance south of the

487   island in the MC and the equator in the tropical WP reflects the southward shift of the

488   MJO deep convection when passing through the MC, partly due to the blocking effect

489   of mountainous islands and the higher moisture content over high SST south of the

490   equator in the region during boreal winter (Kim et al., 2017; Ling et al., 2019; Sobel

491   et al., 2008; Tseng et al., 2017; Wu and Hsu, 2009). Although the control coupled

492   experiment failedfails to simulate the variance maximum in the tropical eastern IO, it

493   appropriately simulatedsimulates the maximum variance over the tropical WP,

494   reflecting its ability to simulate the eastward propagation of the MJO through the MC.

495   By contrast, the uncoupled A–CTL experiment simulatedsimulates considerably

496   weaker intraseasonal variance in both the tropical eastern IO and the tropical WP.

497   Figure 4j–l are the 20–100-day filtered SST (K, shaded) and 850-hPa wind (m s^{-1},

498   vector) during MJO phase 7 when deep convection is the strongest over the dateline.

499 The coupled experiment C–30NS realistically ~~simulated~~simulates the negative SST

500 anomaly over the MC and WP when enhanced tropical convection passed through

501 the MC to the dateline, indicating the capability of the SIT model to reproduce the

502 ~~observed~~ SST anomaly by exchanging ~~surface fluxes~~LHF/SHF between the

503 atmosphere and ocean. In A-CTL, no SST anomaly ~~was~~is evident because the model

504 was forced by prescribed climatological SST. The contrast seen in Fig. 4j–l

505 demonstrates the essential role of atmosphere–ocean coupling in shaping the MJO.

506 A delayed air–sea interaction mechanism was noted, where a preceding active-phase

507 MJO may trigger an inactive-phase MJO through the delayed effect of the induced

508 SST anomaly. In addition, the westerly winds at 850 hPa moving southward between

509 MC and WP ~~were~~are captured by the control experiment C–30NS and ~~were~~are

510 similar to the ~~observed~~ERA-I reanalysis winds (Fig. 4j and 4k). By contrast, A–CTL

511 forced by climatological monthly SST (<0.05 K phase^{-1} anomaly) ~~failed~~fails to

512 simulate the southward westerly wind of the region extending from the MC to the

513 dateline (Fig. 4l).

514

515 4.~~2~~3.2   **Effect of upper-ocean vertical resolution**

516   In the control coupled experiment C–30NS, the vertical resolution in the upper

517 10.~~5~~ m was 1 m. Tseng et al. (2014) suggested that fine vertical resolution is crucial

518 for appropriately simulating the eastward propagation. To investigate the effect of

519 vertical resolution, two ~~coarse-resolution~~ experiments with a thicker first layer were

520 conducted~~, which involved increasing~~ by moving the ~~thickness~~center of the ~~first ocean~~

521 ~~layer (under the cool skin~~ layer) to 11.~~8~~5 m (C–LR12m) and ~~34.2~~33.9 m (C–LR34m),

522 respectively~~.~~, as opposed to the control experiment in which 10 layers were

523 implemented in the first 10.5 meters (see supplementary Fig. S1 for vertical

524 discretization). The W–FS spectral peaks of U850 in C–LR12m ~~were~~are concentrated

525 in eastward-propagating wavenumber 1 at three timescales (e.g., longer than 80 days,

526 30–80 days, and approximately 30 days; Fig. 5a). In C–LR34m, both eastward and

527 westward signals ~~were~~are simulated with the dominant W–FS timescale ~~that was~~

528 longer than 80 days (Fig. 5b). The appearance of both eastward and westward signals

529 at a lower frequency implied a stronger stationary tendency or weaker eastward-

530 propagating tendency. This result is consistent with that reported by Tseng et al.

531 (2014) that the scientific reproducibility of coarser ~~the~~ resolution ~~is, the~~causes a

532 longer intraseasonal periodicity and slower ~~is the~~ eastward propagation of the MJO.

533   The effect of vertical resolution on the MJO simulation can be seen in the

534 Hovmöller diagram. The eastward propagation simulated in C–LR12m (Fig. 5c)

535 markedly weakened after crossing the MC ~~compared~~compare with that simulated in

536 the control experiment C–30NS~~.~~ (Fig. 2e). In C–LR34m, the quasi-stationary

537 fluctuation and westward propagation ~~were~~are simulated over the IO (Fig. 5d),

538 appearing similar to those in A–CTL~~.~~ (Fig. 2f). The ~~observed~~ lead–lag relationship

539 between precipitation (zonal wind) and SST ~~was~~is poorly simulated in C–LR12m

540 (Fig. 5e) and even more poorly simulated in C–LR34m (Fig. 5f). This result confirms

541 the finding reported by Tseng et al. (2014) that a higher vertical resolution in the

542 ~~first~~upper few meters below the surface allows for a faster air–sea interaction, thus

543 resulting in a more realistic simulation of the MJO.

544

545 **4**3**.3 Effect of the lowest boundary of the SIT model**

546   The ocean is a vital energy source for the MJO. Although vertical resolution is

547 crucial for the efficiency of air–sea interaction, the thickness of the upper ocean that

548 interacts with the atmosphere represents the ocean heat content to substantiate the

549 MJO. A key question is how thick ~~an oceanic~~a vertically-gridded ocean mixed layer

550 should be for a realistic simulation. To explore this issue, three experiments with a

551 model ocean with a 1-m vertical resolution and the ocean model (SIT) bottom at 10,

552 30, and 60 m, which included the top ~~11, 13~~12, 14, and ~~15~~16 levels, respectively, as

553 ~~listed~~shown in ~~Section 2~~supplementary Fig. S2 and Table 1, were conducted. The

554 spectra and the Hovmöller diagrams shown in Fig. 6a–c and Fig. 6d–f, respectively,

555 demonstrate that the thicker ocean model ~~ocean simulated~~simulates a stronger MJO

556 with a frequency closer to those in the ~~observation and an~~coupled experiment C–

557 30NS and ERA-I/NOAA data, and more realistic eastward propagation ~~similar to that~~

558 ~~in C–30NS and observations.~~. In addition, the lead–lag relationship between

559 precipitation (wind) and SST ~~was~~is more realistically simulated with increasing

560 thickness of the ocean model (Fig. 6g–i).

561   This result suggests that the thickness of the ~~upper ocean~~oceanic mixed layer that

562 interacts with the atmosphere strongly affects the frequency of the simulated MJO. A

563 thinner (thicker) oceanic mixed layer is more quickly (slowly) recharged and

564 discharged through ~~heat~~SHF and LHF exchange between the atmosphere and ocean

565 and therefore likely fluctuates at a faster (slower) tempo. The simulated periodicity is

566 therefore affected by the thickness of oceanic mixed layer (or ocean heat content).

567 Although ~~this study~~the result suggests 60 m is an appropriate thickness to realistically

568 simulate the periodicity of the MJO, we did not intend to suggest the exact thickness

569 required for a proper simulation because it might depend on the model. The oceanic

570 mixed layer should be adequately thick to contain a certain amount of heat to generate

571 appropriate periodicity ~~that is close to that observed~~. However, the reason for the

572 intraseasonal time scale (i.e., 20-100 days) should be determined in future studies.

573 This finding does not suggest a constant periodicity because periodicity might be

574 affected by the time-varying structure of the atmosphere and ocean in the real world.

575

576 **~~4~~3.4 Effects of coupling domains**

577   The MJO is a planetary-scale phenomenon. Given its large-scale circulation, the

578   air–sea interaction affecting the MJO likely occurs in a much larger area than the

579   region near the major convection anomalies. In this section, we discuss ~~whether and~~

580   ~~how~~ the effect of coupling domain ~~affects a~~on model~~'s~~ ability to simulate the eastward

581   propagation speed and periodicity of the MJO. Four experiments considering the

582   coupling in various domains (C–0_30N, C–0_30S, C–30_180E, and C–30E_75W,

583   Fig. 1) were conducted ~~to investigate~~for the ~~effect of the coupling domain on the~~

584   ~~eastward propagation speed and periodicity of the MJO in the simulation.~~purpose.

585   The results are shown in Fig. 7. ~~The domains of the four experiments are shown in~~

586   ~~Fig. 1.~~ The C–0_30N that considered the coupling in the tropics between the equator

587   and 30°N ~~simulated~~simulates the least realistic MJO propagation in terms of W–FS

588   (Fig. 7a), zonal wind–precipitation coupling (Fig. 7e), and SST–precipitation (Fig.

589   7i) ~~of~~among the four regional coupling experiments. By contrast, coupling only the

590   tropics between the equator and 30°S ~~simulated~~simulates a more realistic MJO in all

591   three aspects (i.e., spectrum in Fig. 7b, temporal evolution of precipitation/wind, and

592   precipitation/SST coupling in Fig. 7f and 7j). Figure. 8a indicates that the ~~positive~~

593   ~~precipitation~~negative OLR anomalies at phase 5 simulated in C–0_30N ~~stayed~~stays

594   mainly north of the equator and ~~did~~does not shift southward in the MC as

595   ~~observed~~revealed in ERA-I reanalysis and ~~in~~NOAA OLR and in the control

596   experiment C–30NS, and the convection over the IO ~~was~~is unrealistically weak. By

597   contrast, the southward detouring in the MC ~~was~~is realistically simulated in C–0_30S

598   that coupled only the tropical ocean between the equator and 30°S. This result

599   indicates that air–sea coupling occurring south of the equator is the key to producing

600   appropriate eastward propagation and detouring of the MJO through the MC. Without

601   this coupling, the C–0_30N experiment ~~failed~~fails to realistically simulate the

602   eastward propagation of the MJO~~.~~ (Fig. 7e). This contrast can be attributed to the

603 ~~observed~~ warmer ocean surface and higher moisture content found south of the

604 equator in boreal winter, which comprise a more favorable environmental condition

605 for air–sea coupling and convection–circulation coupling and the occurrence of the

606 MJO.

607   MJO simulations can be affected by air–sea coupling in the longitudinal domain.

608 Tseng et al. (2014) examined this effect by allowing coupling in different regions

609 (e.g., the IO, WP, and IO + WP) and found that the IO + WP coupling experiment

610 yielded the most satisfactory MJO simulation in terms of the zonal W–FS and

611 eastward propagation characteristics. In this study, we conducted sensitivity

612 experiments in which we allowed coupling in the tropics in two longitudinal domains,

613 namely 30°E–180°E (C–30_180E) and 30°E–75°W (C–30E_75W). The 30°E–180°E

614 region covered the IO and WP, and the 30°E–75°W region covered the IO and the

615 entire tropical Pacific. As shown in Fig. 7, the C–30E_75W experiment ~~simulated the~~

616 ~~MJO, yielding results~~simulates more ~~similar to the observation and those in C–~~

617 ~~30NS~~realistic MJO than ~~to~~the C–30_180E experiment, with stronger eastward

618 propagation and larger amplitudes in the spectrum (Fig. 7c and 7d) and Hovmöller

619 diagrams of precipitation/wind (Fig. 7g and 7h) and precipitation/SST (Fig. 7k and

620 7l). The simulated MJO in C–30E_75W propagated ~~further~~farther east than that in C–

621 30_180E, particularly evident in Fig. 7k and 7l. The spatial distributions of circulation

622 and ~~precipitation~~OLR shown in Fig. 8c and 8d ~~indicated~~indicate the presence of a

623 stronger convective-coupled circulation system over the MC and WP in C–30E_75W.

624 These results suggest that coupling over the entire tropical IO and Pacific could

625 enhance the strength and eastward propagation of the MJO and encourage

626 ~~further~~farther propagation to the central Pacific.

627

628 **4~~3~~.5 Diurnal versus no diurnal cycle in air–sea coupling**

629   ~~The~~Previous studies showed that the diurnal cycle in the MC can weaken the

630   MJO and its eastward propagation (Hagos et al., 2016; Oh et al., 2013). We conducted

631   an experiment to determine whether ~~the~~computing surface heat fluxes using daily

632   mean ~~value~~values, instead of instantaneous values, of atmospheric variables and SST

633   with the same coupling frequency would affect the MJO simulation. The coupling in

634   the model was ~~performed~~conducted through ~~heat flux~~the SHF and LHF exchange

635   between the atmosphere and ocean~~.~~, that were calculated based on simulated winds,

636   moisture, and temperature. As mentioned in Section 2.3, air–sea fluxes were

637   calculated twice for every time step (coupling 48 times per day~~,~~) in the control

638   coupled experiment (C–30NS) based on the instantaneous values of atmospheric and

639   oceanic variables. In the experiment in which the diurnal cycle was removed (C–

640   30NS–nD), air–sea fluxes were calculated as in C–30NS but were based on daily

641   ~~mean data.~~means of both atmospheric variables and SST. Doing this removed certain

642   diurnal effects of air-sea coupling. The results shown in Fig. 9 reveal the enhancement

643   of the eastward-propagating signals in the MJO (e.g., a larger amplitude in spectrum;

644   Fig. 9a) and further eastward ~~and faster~~propagation (Fig. 9b) as well stronger

645   coupling between precipitation and SST (Fig. 9c~~).~~) in C–30NS–nD. The overall

646   results are consistent with previous finding that the diurnal cycle tends to reduce the

647   amplitude ~~and propagation~~of the MJO, indicating that the weakening effect occurs

648   through air–sea coupling in addition to those processes in the atmosphere. Previous

649   studies have hypothesized that rapid interaction processes in the diurnal time scale

650   tend to extract energy from the MJO, thus reducing ~~both~~the strength and propagation

651   tendency of the MJO. However, a comparison between the spectra of C–30NS and C–

652   30NS–nD ~~indicated~~indicates that the experiment in which the diurnal cycle ~~was~~is

653   removed appeared to oversimulate the MJO with unrealistic strength, suggesting that

654   the effect of the diurnal cycle should be considered in the model to simulate a more

655   realistic MJO. However, whether this is a common result in different models remain

656   to be examined.

657   ——

658

659   ~~5~~ **4. Discussion and conclusions**

660   Air–sea coupling is a key mechanism for the successful simulation of the MJO

661   (Chang et al., 2019; DeMott et al., 2015; Jiang et al., 2015, 2020; Kim et al., 2010; Li

662   et al., 2016; Li et al., 2020; Newman et al., 2009; Tseng et al., 2014). This study,

663   following the study ~~conducted by~~of Tseng et al. (2014), demonstrated that coupling a

664   high-resolution 1-D TKE ocean model (namely the SIT model) to the CAM5, namely

665   the CAM5–SIT, significantly improved the MJO simulation over the standalone

666   CAM5. ~~The CAM5–SIT realistically simulated~~By coupling SIT model to an AGCM

667   different from Tseng et al. (2014), this study confirms the scientific reproducibility for

668   the improvement of MJO simulation in modeling science. The CAM5–SIT

669   realistically simulates the MJO characteristics in many aspects (e.g., intraseasonal

670   periodicity, eastward propagation, coherence in the low-frequency band, detouring

671   propagation across the MC, tilting vertical structure, and intraseasonal variance in the

672   WP).

673   Systematic sensitivity experiments were conducted to investigate the effects of

674   the vertical resolution and the thickness of the 1-D ocean model, coupling domains,

675   and the absence of the diurnal cycle. The results of all the sensitivity experiments are

676   summarized in Fig. 10a and 10b, which show four common metrics for MJO

677   evaluation. The four metrics are the propagation speed of the MJO (estimated from

678   the U850 Hovmöller diagram as Fig. 2d–f) versus the power ratio of eastward- and

679   westward-propagating 30–80-day signals (E/W ratio, derived from the zonal W–FS)

680   in Fig. 10a– and the eastward propagation speed of the 30–80-day filtered

681   precipitation anomaly (estimated from the precipitation Hovmöller diagram) versus

682   the variance explained by RMM1 and RMM2 (i.e., the sum of the variance explained

683   by EOF1 and EOF2 based on Wheeler and Hendon, 2004) in Fig. 10b. Based on the

684   maximum precipitation anomaly and zero values of U850 (indicating deep convection

685   region), propagation speeds of precipitation and U850 were calculated from

686   Hovmöller diagrams between 60°E and 150°W. Overall, the control experiment C–

687   30NS simulates the most realistic MJO among all sensitivity experiments.

688   As for vertical resolution, we determined that the MJO simulation efficiency

689   decreased when the vertical resolution of the SIT model wasis decreased from 1 m to

690   12 or 34 m, as observedsimulated in the C–LR12m and C–LR34m experiments,

691   respectively. This finding, consistent with that reported by Tseng et al. (2014),

692   suggests that a finer vertical resolution more effectively resolves temperature

693   variations in the ocean warm layer and enhances atmospheric–ocean coupling, thus

694   enabling the upper ocean to more efficiently respond to atmospheric forcing by

695   providing sensible and latent heat fluxes; this results in superior synchronization

696   between the lower atmosphere and the upper ocean.

697   We observed that the thinnershallower ocean mixed layermodel bottom could

698   speed up the eastward propagation of the MJO by producing more perturbations of

699   shorter periodicity (Fig. 6) and resultedresults in a weaker MJO. The shallower

700   oceanic mixed layer likely respondedresponds more quickly to atmospheric forcing

701   but providedprovides less sensible and latent heat fluxes to the atmosphere. Thus, the

702   MJO propagatedpropagates too fast with a weaker amplitude.

703   In the coupling domain sensitivity experiments, we investigated the essential

704   coupling domain required to simulate the realistic MJO and the effect of the domain

705   on the MJO simulation. Coupling only the northern tropics failedfails to simulate the

706   eastward propagation, whereas coupling only the southern tropics yieldedyields a

707 more realistic MJO simulation, although this simulation ~~was~~is inferior to coupling the

708 entire tropics. This contrast reveals the importance of the southern tropical ocean,

709 especially in the MC where high SST and moisture content are noted. Coupling in the

710 southern tropics is therefore essential for providing the energy required to maintain

711 the MJO and its eastward propagation. By contrast, the northern tropics are relatively

712 dry and cool. Coupling in this region is therefore less effective in improving MJO

713 simulation.

714   In the longitudinal domain sensitivity experiments, we found that the MJO

715 amplitude and the eastward extend of its eastward propagation ~~were~~are enhanced by

716 extending the eastern boundary of the coupling domain from the tropical eastern IO to

717 the tropical WP and further to the tropical eastern Pacific (Fig. 1). Further extension

718 of the domain to cover the tropical Atlantic ~~did~~does not exhibit further enhancement

719 (not shown). This result indicates that coupling in the tropical central and eastern

720 Pacific, although not the major MJO signal regions (i.e., from the tropical IO to the

721 tropical WP), still played a marked role in sustaining the MJO. We propose the

722 following to explain this effect. Because of the planetary scale of the MJO, the near-

723 surface easterly circulation to the east of the convection core often extended to the

724 tropical central and eastern Pacific where the climatological easterly prevailed. The

725 coupling beyond the WP increased low-level moisture transport and convergence to

726 the east of the convection and establish an environment suitable for the further

727 eastward propagation of the MJO. This effect was likely terminated by the landmass

728 of Central America when the tropical Atlantic was further included. Thus, a further

729 eastward extension of the coupling domain exerted little effect on further enhancing

730 the MJO. A diagnostic study on the effect of the longitudinal coupling domain is

731 being conducted, and the results will be reported in a following paper.

732   The diurnal versus nondiurnal cycle experiment ~~indicated~~indicates that

733 nondiurnal coupling tended to enhance eastward-propagating signals but slow down

734 the eastward propagation. (Fig. 10a–b). This result is consistent with the finding of

735 previous studies that the diurnal cycle in the atmosphere extracts energy from the

736 MJO, thus weakening it.

737   In this study, we demonstrated how air–sea coupling can improve the MJO

738 simulation in a GCM. The findings are as follows.

739 (1) Better resolving the fine structure of the upper-ocean temperature and therefore

740   the air–sea interaction ledleads to more realistic intraseasonal variability in both

741   SST and atmospheric circulation.

742 (2) An adequate thickness of the oceanic mixed layer is required to simulate a delayed

743   response of the upper ocean to atmospheric forcing and lower-frequency

744   fluctuation.

745 (3) Coupling the tropical eastern Pacific, in addition to the tropical IO and the tropical

746   WP, can enhance the MJO and facilitate the further eastward propagation of the

747   MJO to the dateline.

748 (4) Coupling the southern tropical ocean, instead of the norther tropical ocean, is

749   essential for simulating a realistic MJO.

750 (5) Stronger MJO variability can be obtained without considering the diurnal cycle in

751   coupling.

752   Our study confirmed the effectiveness of air–sea coupling for improving MJO

753 simulation in a climate model and demonstrated how and where to couple. The

754 findings enhance our understanding of the physical processes that shape the

755 characteristics of the MJO.

756

757 *Code and data availability.* The model code of CAM5–SIT is available at

758 https://doi.org/10.5281/zenodo.5510795. Input data of CAM5–SIT using the

759   climatological Hadley Centre Sea Ice and Sea Surface Temperature dataset and

760   GODAS data forcing, including 30-year numerical experiments, are available at

761   https://doi.org/10.5281/zenodo.5510795.

762

763   *Author contributions.* HHH is the initiator and the primary investigator of the

764   Taiwan Earth System Model project. YYL is the CAM5–SIT model developer and

765   writes the majority part of the paper. WLT and LCJ assist in MJO analysis.

766

767   *Competing interests.* The authors declare that they have no conflict of interest.

768

769   *Acknowledgements.* The contribution from YYL, HHH, WLT, and LCJ to this study is

770   supported by Ministry of Science and Technology of Taiwan under contracts MOST

771   110-2123-M-001-003, MOST 110-2811-M-001-603, MOST 109-2811-M-001-624

772   and MOST108-2811-M-001-643. Our deepest gratitude goes to the editors and

773   anonymous reviewers for their careful work and thoughtful suggestions that have

774   helped improve this paper substantially. We sincerely thank the National Center for

775   Atmospheric Research and their Atmosphere Model Working Group (AMWG) for

776   release CESM1.2.2. We thank the computational support from National Center for

777   High530 performance Computing of Taiwan. This manuscript was edited by Wallace

778   Academic Editing.

779

780   **Reference**
781   Adler, R. F., Huffman, G. J., Chang, A., Ferraro, R., Xie, P.
782   P., Janowiak, J., Rudolf, B., Schneider, U., Curtis, S., Bolvin,
783   D., Gruber, A., Susskind, J., Arkin, P., and Nelkini, E.: The
784   Version 2.1 Global Precipitation Climatology Project (GPCP)
785   Monthly Precipitation Analysis (1979 -Present), J. Hydrometeor.,
786   4(6), 1147-1167, https://doi.org/10.1175/1525-
787   7541(2003)004<1147:TVGPCP>2.0.CO;2, 2003.

788   Ahn, M.-S., Kim, D., Kang, D., Lee, J., Sperber, K. R., and Glecker, P.

789 J., et al.: MJO propagation across the Maritime Continent: Are
790 CMIP6 models better than CMIP5 models? Geophys. Res. Lett., 47,
791 e2020GL087250, https://doi.org/10.1029/2020GL087250, 2020.

792 Ahn, M.-S., Kim, D., Sperber, K. R., Kang, I.-S., Maloney, E., Waliser,
793 D., and Hendon, H.: MJO simulation in CMIP5 climate models:
794 MJO skill metrics and process-oriented diagnosis, Clim.
795 Dyn., 49, 4023–4045, https://doi.org/10.1007/s00382-017-3558-4,
796 2017.

797 Alappattu, D. P., Wang, Q., Kalogiros, J., Guy, N., and Jorgensen, D.
798 P.: Variability of upper ocean thermohaline structure during a MJO
799 event from DYNAMO aircraft observations, J. Geophys. Res. -
800 Oceans, 122, 1122–1140, https://doi.org/10.1002/2016JC012137,
801 2017.

802 Amante, C., and Eakins, B. W.: ETOPO1 1 arc-minute globe relief
803 model: Procedures, data sources and analysis, NOAA Tech. Memo.
804 NESDIS NGDC-24, 19 pp., NOAA, Silver Spring, Md., 2009.

805 Behringer, D. W., and Xue, Y.: Evaluation of the global ocean data
806 assimilation system at NCEP: The Pacific Ocean. Eighth
807 Symposium on Integrated Observing and Assimilation Systems for
808 Atmosphere, Oceans, and Land Surface, AMS 84th Annual
809 Meeting, Washington State Convention and Trade Center, Seattle,
810 Washington, 11-15. Derber, J.C., and A. Rosati, 1989: A global
811 oceanic data assimilation system, J. Phys. Oceanogr., 19, 1333–
812 1347, https://ams.confex.com/ams/pdfpapers/70720.pdf, 2004.

813 Bentsen, M., Bethke, I., Debernard, J. B., Iversen, T., Kirkevåg, A.,
814 Seland, Ø., Drange, H., Roelandt, C., Seierstad, I. A., Hoose, C.,
815 and Kristjánsson, J. E.: The Norwegian Earth System Model,
816 NorESM1-M – Part 1: Description and basic evaluation of the
817 physical climate, Geosci. Model Dev., 6, 687–720,
818 https://doi.org/10.5194/gmd-6-687-2013, 2013.

819 Bernie, D., Guilyardi, E., Madec, G., Slingo, J., Woolnough, S., and
820 Cole, J.: Impact of resolving the diurnal cycle in an ocean–
821 atmosphere GCM. Part 2: a diurnally coupled CGCM, Clim.
822 Dynam., 31, 909–925, https://doi.org/10.1007/s00382-008-0429-z,
823 2008.

824 Boyle, J. S., Klein, S. A., Lucas, D. D., Ma, H.-Y., Tannahill, J., and
825 Xie, S.: The parametric sensitivity of CAM5's MJO, J. Geophys.
826 Res.-Atmos., 120, 1424–1444,
827 https://doi.org/10.1002/2014JD022507, 2015.

828 Bui, H. X., and Maloney, E. D.: Changes in Madden-Julian Oscillation
829 precipitation and wind variance under global warming, Geophys.
830 Res. Lett., 45, 7148–7155, https://doi.org/10.1029/2018GL078504,
831 2018.

832 Chang, M.-Y., Li, T., Lin, P.-L., and Chang, T.-H.: Forecasts of MJO

833 Events during DYNAMO with a Coupled Atmosphere-Ocean
834 Model: Sensitivity to Cumulus Parameterization Scheme, J.
835 Meteorol. Res., 33, 1016–1030, https://doi.org/10.1007/s13351-
836 019-9062-5, 2019.

837 CLIVAR MADDEN–JULIAN OSCILLATION WORKING GROUP:
838 MJO simulation diagnostics, J. Climate, 22, 3006–3030,
839 https://doi.org/10.1175/2008JCLI2731.1, 2009.

840 Crueger, T., Stevens, B., and Brokopf, R.: The Madden–Julian
841 Oscillation in ECHAM6 and the introduction of an objective MJO
842 metric, J. Climate, 26, 3241–3257, https://doi.org/10.1175/JCLI-D-
843 12-00413.1, 2013.

844 Danabasoglu, G., Lamarque, J.-F., Bacmeister, J., Bailey, D. A.,
845 DuVivier, A. K., and Edwards, J., et al.: The Community Earth
846 System Model Version 2 (CESM2), J. Adv. Model. Earth Syst., 12,
847 e2019MS001916, https://doi.org/10.1029/2019MS001916, 2020.

848 Dee, D. P., Uppala, S. M., Simmons, A. J., Berrisford, P., Poli, P.,
849 Kobayashi, S., Andrae, U., Balmaseda, M. A., Balsamo, G., Bauer,
850 P., Bechtold, P., Beljaars, A. C. M., van de Berg, L., Bidlot, J.,
851 Bormann, N., Delsol, C., Dragani, R., Fuentes, M., Geer, A. J.,
852 Haimberger, L., Healy, S. B., Hersbach, H., Hólm, E. V., Isaksen,
853 L., Källberg, P., Köhler, M., Matricardi, M., McNally, A. P.,
854 Monge-Sanz, B. M., Morcrette, J.-J., Park, B.-K., Peubey, C., de
855 Rosnay, P., Tavolato, C., Thépaut, J.-N., and Vitart, F.: The ERA-
856 Interim reanalysis: configuration and performance of the data
857 assimilation system, Q. J. R. Meteorol. Soc., 137: 553–597,
858 https://doi.org/10.1002/qj.828, 2011.

859 de Szoeke, S. P., Skyllingstad, E. D., Zuidema, P., and Chandra, A.
860 S.: Cold pools and their influence on the tropical marine boundary
861 layer, J. Atmos. Sci., 74, 1149–1168. https://doi.org/10.1175/JAS-
862 D-16-0264.1, 2017.

863 Delworth, T. L., et al.: GFDL's CM2 global coupled climate models.
864 Part 1: Formulation and simulation characteristics, J. Climate, 19,
865 643–674, https://doi.org/10.1175/JCLI3629.1, 2006.

866 DeMott, C. A., Klingaman, N. P., and Woolnough, S. J.: Atmosphere-
867 ocean coupled processes in the Madden-Julian oscillation, Rev.
868 Geophys., 53, 1099–1154, https://doi.org/10.1002/2014RG000478,
869 2015.

870 DeMott, C. A., Klingaman, N. P., Tseng, W.-L., Burt, M. A., Gao, Y.,
871 and Randall, D. A.: The convection connection: How ocean
872 feedbacks affect tropical mean moisture and MJO propagation, J.
873 Geophys. Res.-Atmos., 124, 11,910–11,931,
874 https://doi.org/10.1029/2019JD031015, 2019.

881 Gaspar, P., Gregoris, Y., and Lefevre, J.-M.: A simple eddy kinetic
882 energy model for simulations of the oceanic vertical mixing: tests

at station papa and long-term upper ocean study site, J. Geophys. Res. -Oceans, 95, 16179–16193, https://doi.org/10.1029/JC095iC09p16179, 1990.

Gonzalez, A. O., and Jiang, X.: Winter mean lower tropospheric moisture over the Maritime Continent as a climate model diagnostic metric for the propagation of the Madden-Julian oscillation, Geophys. Res. Lett., 44, https://doi.org/10.1002/2016GL072430, 2017.

Grassl, H.: The dependence of the measured cool skin of the ocean on wind stress and total heat flux, Bounday-Layer Meteorol., 10, 465–474, https://doi.org/10.1007/BF00225865, 1976.

Haertel, P.: Prospects for Erratic and Intensifying Madden-Julian Oscillations, Climate, 8, 24, https://doi.org/10.3390/cli8020024, 2020.

Hannah, W. M., and Maloney, E. D.: The moist static energy budget in NCAR CAM5 hindcasts during DYNAMO, J. Adv. Model. Earth Syst., 6, 420–440, https://doi.org/10.1002/2013MS000272, 2014.

Hasse, L.: The sea surface temperature deviation and the heat flow at the sea-air interface, Bounday-Layer Meteorol., 1, 368–379, https://doi.org/10.1007/BF02186037, 1971.

Hagos, S. M., Zhang, C., Feng, Z., Burleyson, C. D., Mott, C. De, Kerns, B., Benedict, J. J., and Martini, M. N.: The impact of the diurnal cycle on the propagation of Madden-Julian Oscillation convection across the Maritime Continent, J. Adv. Model. Earth Syst., 8, 1552–1564, https://doi.org/10.1002/2016MS000725, 2016.

He, S., Yang, S., and Li, Z.: Influence of Latent Heating over the Asian and Western Pacific Monsoon Region on Sahel Summer Rainfall, Sci. Rep. 7, 7680, https://doi.org/10.1038/s41598-017-07971-6, 2017.

Heath, A., Gonzalez, A. O., Gehne, M., and Jaramillo, A.: Interactions of large-scale dynamics and Madden-Julian Oscillation propagation in multi-model simulations, J. Geophys. Res.-Atmos., 126, e2020JD033988. https://doi.org/10.1029/2020JD033988, 2021.

Hong, X., Reynolds, C. A., Doyle, J. D., May, P., and O'Neill, L.: Assessment of upper-ocean variability and the Madden-Julian Oscillation in extended-range air–ocean coupled mesoscale simulations, Dyn. Atmos. Oceans, 78, 89–105. https://doi.org/10.1016/j.dynatmoce.2017.03.002, 2017.

Hung, M.-P., Lin, J.-L., Wang, W., Kim, D., Shinoda, T., and Weaver, S. J.: MJO and convectively coupled equatorial waves simulated by CMIP5 climate models, J. Climate, 26, 6185–6214, https://doi.org/10.1175/JCLI-D-12-00541.1, 2013.

Hurrell, J. W., Holland, M. M., Gent, P. R., Ghan, S., Kay, J. E.,

Kushner, P. J., Lamarque, J.-F., Large, W. G., Lawrence, D., Lindsay, K., Lipscomb, W. H., Long, M. C., Mahowald, N., Marsh, D. R., Neale, R. B., Rasch, P., Vavrus, S., Vertenstein, M., Bader, D., Collins, W. D., Hack, J. J., Kiehl, J., and Marshall, S.: The community Earth system model: A framework for collaborative research, B. Am. Meteorol. Soc., 94, 1319–1360, https://doi.org/10.1175/BAMS-D-12-00121, 2013.

Jiang, X., et al.: Vertical structure and physical processes of the MaddenJulian oscillation: Exploring key model physics in climate simulations, J. Geophys. Res.-Atmos., 120, 4718–4748, https://doi.org/10.1002/2014JD022375, 2015.

Jiang, X., Adames, Á. F., Kim, D., Maloney, E. D., Lin, H., and Kim, H., et al.: Fifty years of research on the Madden-Julian Oscillation: Recent progress, challenges, and perspectives, J. Geophys. Res.-Atmos., 125, e2019JD030911, https://doi.org/10.1029/2019JD030911, 2020.

Johnson, R. H., and Ciesielski, P. E.: Multiscale variability of the atmospheric boundary layer during DYNAMO, J. Atmos. Sci., 74, 4003–4021, https://doi.org/10.1175/JAS-D-17-0182.1, 2017.

Kaylor, R. E.: Filtering and decimation of digital time series, Tech. Rep. Note BN 850, Institute for Physical Science and Technology, University of Maryland at College Park, 14 pp, 1997., 1977.

Kim, D., Sobel, A. H., Maloney, E. D., Frierson, D. M., and Kang, I.-S.: A systematic relationship between intraseasonal variability and mean state bias in AGCM simulations, J. Climate, 24, 5506–5520. https://doi.org/10.1175/2011JCLI4177.1, 2011.

Kim, D., Kim H., and Lee, M.-I.: Why does the MJO detour the Maritime Continent during austral summer? Geophys. Res. Lett., 44, 2579–2587, https://doi.org/10.1002/2017GL072643, 2017.

Kim, H.-M., Hoyos, C. D., and Webster, P. J. et al.: Ocean–atmosphere coupling and the boreal winter MJO, Clim Dynam., 35, 771–784, https://doi.org/10.1007/s00382-009-0612-x, 2010.

Kiranmayi, L., and Maloney, E. D.: Intraseasonal moist static energy budget in reanalysis data, J. Geophys. Res., 116, D21117, https://doi.org/10.1029/2011JD016031, 2011.

Lan, Y.-Y., Tsuang, B.-J., Tu, C.-Y., Wu, T.-Y., Chen, Y.-L., and Hsieh, C.-I.: Observation and Simulation of Meteorology and Surface Energy Components over the South China Sea in Summers of 2004 and 2006, Terr. Atmos. Ocean. Sci., 21, 325–342, https://doi.org/ 10.3319/TAO.2009.04.07.01(A), 2010.

Lee, H.-T., and NOAA CDR Program: NOAA Climate Data Record (CDR) of Daily Outgoing Longwave Radiation (OLR), Version 1.2,

970   NOAA National Climatic Data
971   Center, https://doi.org/10.7289/V5SJ1HH2, 2011.

972 Li, T., Ling, J., and Hsu, P.-C.: Madden–Julian Oscillation: Its
973   discovery, dynamics, and impact on East Asia, J. Meteor. Res., 34,
974   20–42, https://doi.org/10.1007/s13351-020-9153-3, 2020.

975 Li, T., Tam, F., Fu, X., Zhou, T., and Zhu, W.: Causes of the
976   intraseasonal SST variability in the tropical Indian Ocean, Atmos.
977   Oceanic Sci. Lett., 1, 18–23,
978   https://doi.org/10.1080/16742834.2008.11446758, 2008.

979 Li, X., Tang, Y., Zhou, L., Chen, D., and Yao, Z.: Assessment of Madden–Julian
980   oscillation simulations with various configurations of CESM, Clim. Dynam.,
981   47, 2667–2690, https://doi.org/10.1007/s00382-016-2991-0, 2016.

982 Ling, J., Zhao, Y., and Chen, G.: Barrier effect on MJO propagation
983   by the Maritime Continent in the MJO Task Force/GEWEX
984   atmospheric system study models, J. Climate, 32, 5529–
985   5547, https://doi.org/10.1175/JCLI-D-18-0870.1, 2019.

986 Madden, R. A., and Julian, P. R.: Description of global-scale
987   circulation cells in the tropics with a 40-50 day period, J. Atmos.
988   Sci., 29, 1109-1123, https://doi.org/10.1175/1520-
989   0469(1972)029<1109:DOGSCC>2.0.CO;2, 1972.

990 Madden, R. A., and Julian, P. R.: Observations of the 40-50 day
991   tropical oscillation - A review, Mon. Weather Rev., 122, 814– 837,
992   https://doi.org/10.1175/1520-
993   0493(1994)122<0814:OOTDTO>2.0.CO;2, 1994.

994 Mellor, G. L., and Yamada, T.: Development of a turbulence closure
995   model for geophysical fluid problems, Rev. Geophys., 20, 851-875,
996   https://doi.org/10.1029/RG020i004p00851, 1982.

997 Neale, R. B., et al.,: Description of the NCAR Community Atmosphere
998   Model (CAM 5.0), NCAR Tech. Note NCAR/TN-486+STR, 289
999   pp., Natl. Cent. for Atmos. Res, Boulder, Colo., 2012.

1000 Newman, M., Sardeshmukh, P. D., and Penland, C.: How important is
1001   air–sea coupling in ENSO and MJO evolution? J.
1002   Clim., 22, 2958– 2977, https://doi.org/10.1175/2008JCLI2659.1,
1003   2009.

1004 Oh, J., Kim, B., and Kim, K. et al.: The impact of the diurnal cycle on
1005   the MJO over the Maritime Continent: a modeling study
1006   assimilating TRMM rain rate into global analysis, Clim.
1007   Dynam., 40, 893–911, https://doi.org/10.1007/s00382-012-1419-8,
1008   2013.

1009 Paulson, C. A. and Simpson, J. J.: The temperature difference across
1010   the cool skin of the ocean, J. Geophys. Res., 86, 11044-11054,
1011   https://doi.org/10.1029/JC086iC11p11044, 1981.

Pei, S., Shinoda, T., Soloviev, A., and Lien, R.-C.: Upper ocean response to the atmospheric cold pools associated with the Madden-Julian Oscillation, Geophys. Res. Lett., 45, 5020–5029, https://doi.org/10.1029/2018GL077825, 2018.

Pujiana, K., Moum, J. N., and Smyth, W. D.: The role of subsurface turbulence in redistributing upper-ocean heat, freshwater, and momentum in response to the MJO in the equatorial Indian Ocean, J. Phys. Oceanogr., 48, 197–220, https://doi.org/10.1175/JPO-D-17-0146.1, 2018.

Rayner, N. A., Parker, D. E., Horton, E. B., Folland, C. K., Alexander, L. V., Rowell, D. P., Kent, E. C., and Kaplan, A.: Global analyses of sea surface temperature, sea ice, and night marine air temperature since the late nineteenth century, J. Geophys. Res., 108(D14), 4407, https://doi.org/10.1029/2002JD002670, 2003.

Ren, P. F., Gao, L., and Ren, H.-L. et al.: Representation of the Madden–Julian Oscillation in CAMSCSM, J. Meteor. Res., 33, 627–650, https://doi.org/10.1007/s13351-019-8118-x, 2019.

Reynolds, R. W., and Smith, T. M.: A high-resolution global sea surface temperature climatology, J. Clim., 8(6),1571–1583, https://doi.org/10.1175/1520-0442(1995)008<1571:AHRGSS>2.0.CO;2, 1995.

Schreck, C. J., Lee, H.-T., and Knapp, K. R.: HIRS outgoing longwave radiation—Daily climate data record: Application toward identifying tropical subseasonal variability, Remote Sens., 10, 1325. https://doi.org/10.3390/rs10091325, 2018.

Sobel, A. H., Maloney, E. D., Bellon, G., and Dargan, M. F.: The role of surface heat fluxes in tropical intraseasonal oscillations, Nat. Geosci., 1, 653–657, https://doi.org/10.1038/ngeo312, 2008.

Subramanian, A. C., Jochum, M., Miller, A. J., Murtugudde, R., Neale, R. B., and Waliser, D. E.: The Madden–Julian oscillation in CCSM4, J. Climate, 24, 6261–6282, https://doi.org/10.1175/JCLI-D-11-00031.1, 2011.

Tseng, W.-L., Tsuang, B.-J., Keenlyside, N. S., Hsu, H.-H. and Tu, C.-Y.: Resolving the upper-ocean warm layer improves the simulation of the Madden-Julian oscillation, Clim. Dynam., 44, 1487–1503, https://doi.org/10.1007/s00382-014-2315-1, 2014.

Tseng, W.-L., Hsu, H.-H., Keenlyside, N., Chang, C.-W. J., Tsuang, B.-J., Tu, C.-Y., and Jiang, L.-C.: Effects of Orography and Land–Sea Contrast on the Madden–Julian Oscillation in the Maritime Continent: A Numerical Study Using ECHAM-SIT, J. Climate, 30, 9725–9741, https://doi.org/10.1175/JCLI-D-17-0051.1, 2017.

Tu, C.-Y., and Tsuang, B.-J.: Cool-skin simulation by a one-column ocean model, Geophys. Res. Lett., 32, L22602, https://doi.org/10.1029/2005GL024252, 2005.

Wang, W., Saha, S., Pan, H.-L., Nadiga, S., and White, G.: Simulation of ENSO in the new NCEP Coupled Forecast System Model (CFS03), Mon. Wea. Rev., 133, 1574–1593, https://doi.org/10.1175/MWR2936.1, 2005.

Wang, W., Hung, M.-P., Weaver, S. J., Kumar, A., and Fu, X.: MJO prediction in the NCEP Climate Forecast System version 2, Clim. Dyn., 42, 2509–2520, https://doi.org/10.1007/s00382-013-1806-9, 2014.

Wheeler, M. C., and Hendon, H. H.: An all-season real-time multivariate MJO index: development of an index for monitoring and prediction, Mon. Weather Rev., 132, 1917–1932, https://doi.org/10.1175/1520-0493(2004)132<1917:AARMMI>2.0.CO;2, 2004.

Wheeler, M., and Kiladis, G. N.: Convectively coupled equatorial waves: Analysis of clouds and temperature in the wavenumber-frequency domain, J. Atmos. Sci., 56, 374– 399, https://doi.org/10.1175/1520-0469(1999)056<0374:CCEWAO>2.0.CO;2, 1999.

Woolnough, S. J., Vitard, F., and Balmaseda, M. A.: The role of the ocean in the Madden–Julian oscillation: Implications for MJO prediction, Quart. J. Roy. Meteor. Soc., 133, 117–128, https://doi.org/10.1002/qj.4, 2007.

Wu, J.: On the cool skin of the ocean, Bounday-Layer Meteorol., 31, 203-207, https://doi.org/10.1007/BF00121179, 1985.

Wu, C.-H., and Hsu, H.-H.: Potential Influence of Topography on the MJO in the Maritime Continent, J. Climate, 22, 5433– 5448, https://doi.org/10.1175/2009JCLI2825.1, 2009.

Yoneyama, K., Zhang, C., and Long, C.: Tracking pulses of the Madden–Julian oscillation, Bull. Amer. Meteor. Soc., 94, 1871–1891, https://doi.org/10.1175/BAMS-D-12-00157.1, 2013.

Zhang, C.: Madden-Julian oscillation, Rev. Geophys., 43, RG2003, https://doi.org/10.1029/2004RG000158, 2005.

Zhang, C., and Yoneyama, K.: CINDY/DYNAMO field campaign: Advancing our understanding of MJO initiation. The Global Monsoon System, C.-P. Chang et al., Eds., In World Scientific Series on Asia-Pacific Weather and Climate, (pp. 339-348). (World Scientific Series on Asia-Pacific Weather and Climate; Vol. Volume 9,), World Scientific Publishing Co., 339– 348,. Pte Ltd. https://doi.org/10.1142/9789813200913_0027, 2017.

1095   Table 1. List of experiments

Section	Category	Experiments	Description
43.1	Coupled or uncoupled	A–CTL	Standalone CAM5.3 forced by ~~observed~~forced by the monthly mean Hadley Centre SST dataset version 1 climatology
		C–30NS (the control coupled experiment)	CAM5.3 coupled with SIT over the tropical domain (30°~~S~~N–30°~~N~~S), with 41 layers of finest vertical resolution (up to ~~submarine topography~~the seabed) and diurnal cycle; the frequency of CAM5 being exchanged with CPL is 48 times per day
43.2	Upper-ocean vertical resolution	C–LR12m	The first ocean vertical level starts at 11.~~8~~5 m with 31 layers (beside SST and cool skin layer are 11.5 m, 29.5 m and 43.6 m up to the seabed)
		C–LR34m	The first ocean vertical level starts at ~~34.2 m~~33.9 m with 28 layers (beside SST and cool skin layer are 33.9 m, 76.9 m and 96.8 m up to the seabed)
43.3	Lowest boundary of SIT	C–HR1mB10m	The lowest boundary of SIT has a depth of 10 m (~~middle grid~~model depth between 0 m and 10 m)
		C–HR1mB30m	The lowest boundary of SIT has a depth of 30 m (~~middle grid~~model depth between 0 m and 30 m)
		C–HR1mB60m	The lowest boundary of SIT has a depth of 60 m (~~middle grid~~model depth between 0 m and 60 m)
43.4	Regional coupling domain in latitude	C–0_30N	Coupled in the tropical northern hemisphere (0°N–30°N, 0°E–360°E)
		C–0_30S	Coupled in the tropical southern hemisphere (0°S–30°S, 0°E–360°E)
	Regional coupling domain in longitude	C–30_180E	Coupled in the Indo-Pacific (30°~~S~~N–30°~~N~~S, 30°E–180°E)
		C–30E_75W	Coupled over the Indian Ocean and Pacific Ocean (30°~~S~~N–30°~~N~~S, 30°E–75°W)
43.5	Absence of the diurnal cycle	C–30NS–nD	Absence of the diurnal cycle in C–30NS; the CAM5.3 daily atmospheric mean of surface wind, temperature, total precipitation, net surface heat flux, u-stress and v-stress over water trigger the SIT and daily mean SST feedback to atmosphere; the frequency of CAM5 is exchanged with CPL 48 times per day

1096   ~~The CAM5.3 AGCM is used in all experiments~~

1097   Experiment abbreviations: "A" means standalone AGCM simulation. "C" means the

1098   CAM5.3 coupled to the SIT model.

1137 zonal wind (contoured, m s^{-1}) averaged over 10°N–10°S, 120–150°E; solid, dashed, and

1138 thick-black curves are positive, negative, and zero values, respectively. (g)–(i) Variation

1139 of 30–60-day filtered precipitation in the eastern IO and the WP in observation (color

1140 shading), and the ratio between intraseasonal and total variance (contoured) and (j)–(l)

1141 composites 20–100-day filtered SST (K, shaded) and 850-hPa winds (m s^{-1}, vector) at

1142 phase 7 when deep convection was the strongest over the dateline. Reference vector

1143 shown at the top right corner of each panel. (a), (d), (g), and (j) are from the

1144 ~~observation~~ERA-I/NOAA data; (b), (e), (h), and (k) are from the control coupled

1145 experiment C–30NS; and (c), (f), (i), and (l) are from the uncoupled experiment A–CTL.

1146

1147 **Figure 5.** (a)–(b) Same as in Fig. 2(a) but for the C–_LR12m and C–_LR34m. (c)–(d)

1148 Same as in Fig. 2(d) but for the C–_LR12m and C–_LR34m. (e)–(f) Same as in Fig. 4(a)

1149 but for the C–_LR12m and C–_LR34m.

1150

1151 **Figure 6.** Same as in Fig. 5 but for the C–HR1mB10m, C–HR1mB30m, and C–

1152 HR1mB60m.

1153

1154 **Figure 7.** Same as in Fig. 5 but for the C–0_30N, C–0_30S, C–30_180E, and C–

1155 30E_75W.

1156

1157 **Figure 8.** Same as in Fig. 3 but for phase 5 in the C–0_30N, C–0_30S, C–30_180E, and

1158 C–30E_75W.

1159

1160 **Figure 9.** Similar as in Fig. 5 but for the C–30NS–nD.

1161

1162 **Figure 10.** Scattered plots of various MJO indices in ~~observation~~the ERA-I/NOAA data

1163 and 12 experiments: (a) power ratio of east/west propagating waves of wavenumber 1–3

1164 of 850-hPa zonal winds (X-axis) with a 30–80-day period and eastward propagation speed

1165 of U850 anomaly (Y-axis) from the Hovmöller diagram and (b) RMM1 and RMM2

1166 variance and eastward propagation speed of the filtered precipitation anomaly derived

1167 from the Hovmöller diagram.
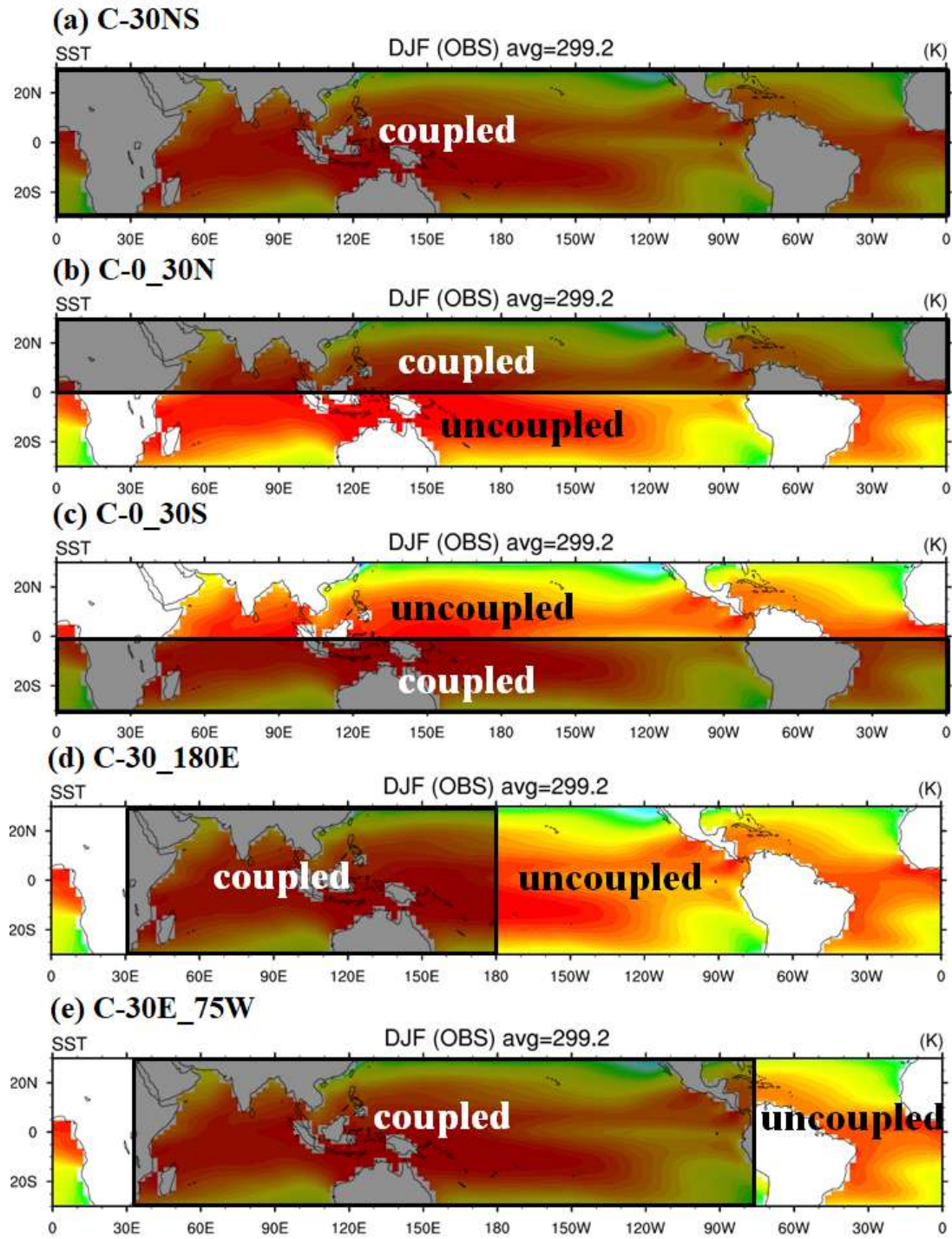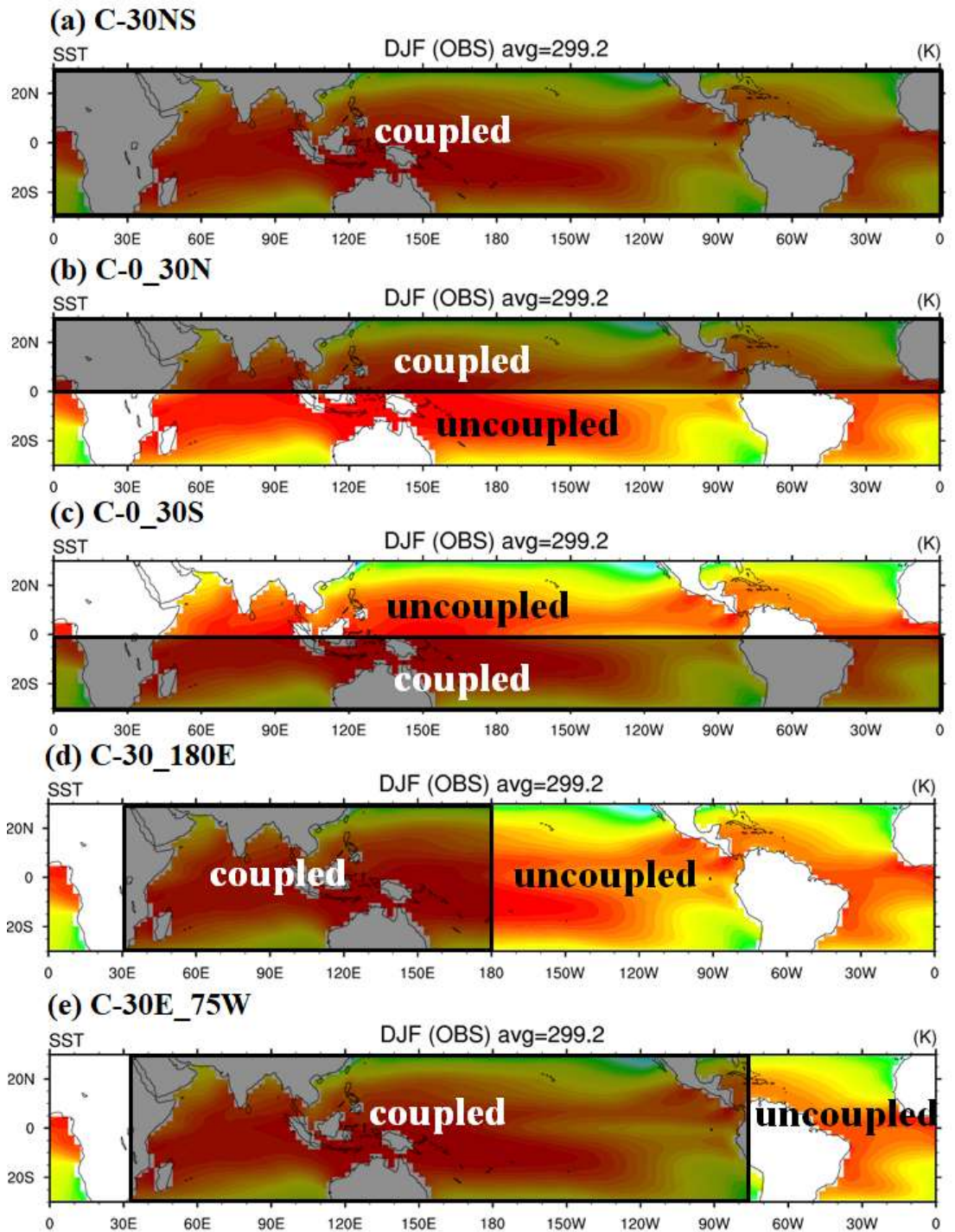
Figure 1. Schematics of coupled and uncoupled domains in the regional coupling experiment: (a) C–30NS, (b) C–0_30N, (c) C–0_30S, (d) C–30_180E, and (e) C–30E_75W. The background is the climatological mean SST in December–February (DJF).
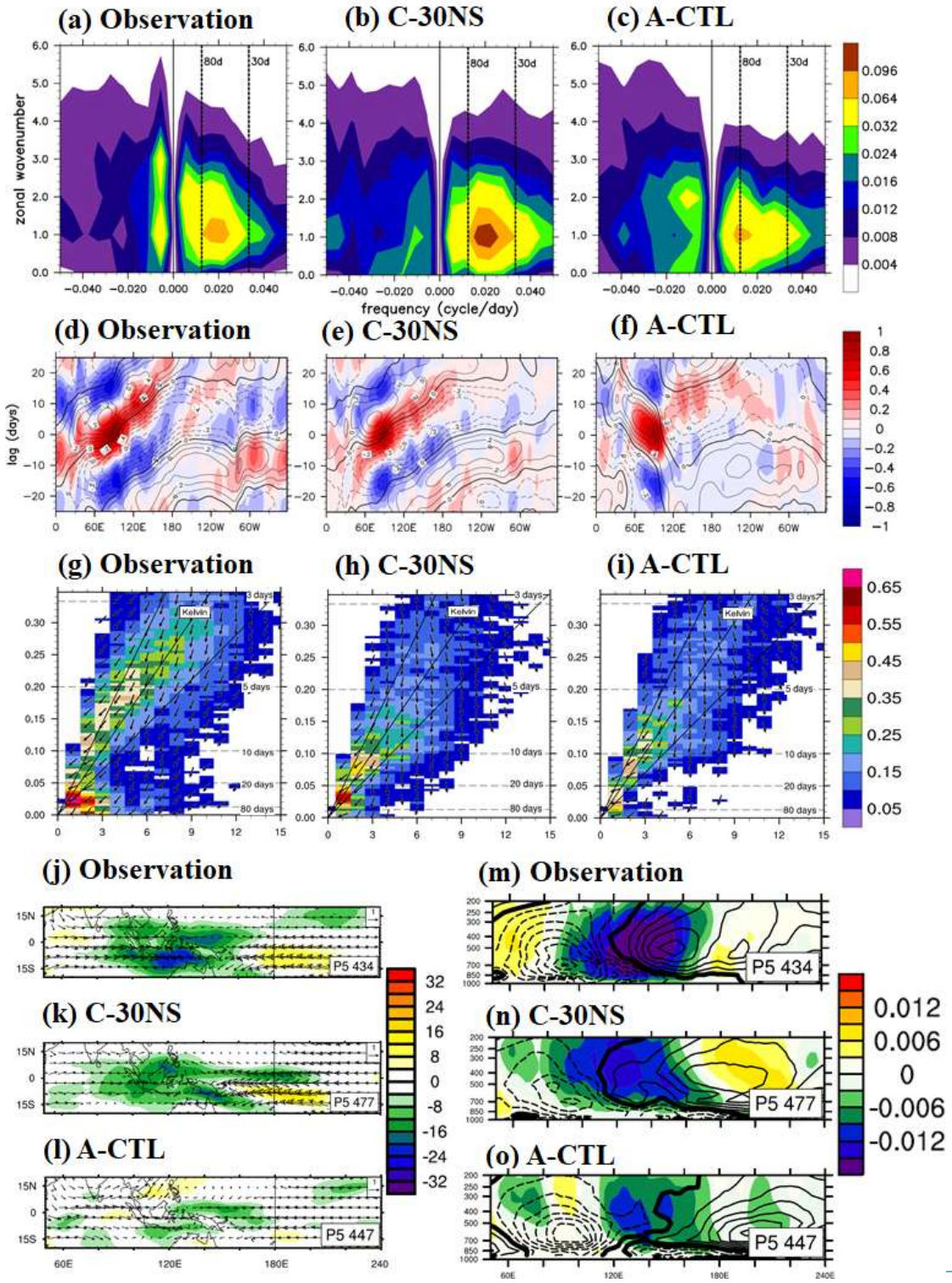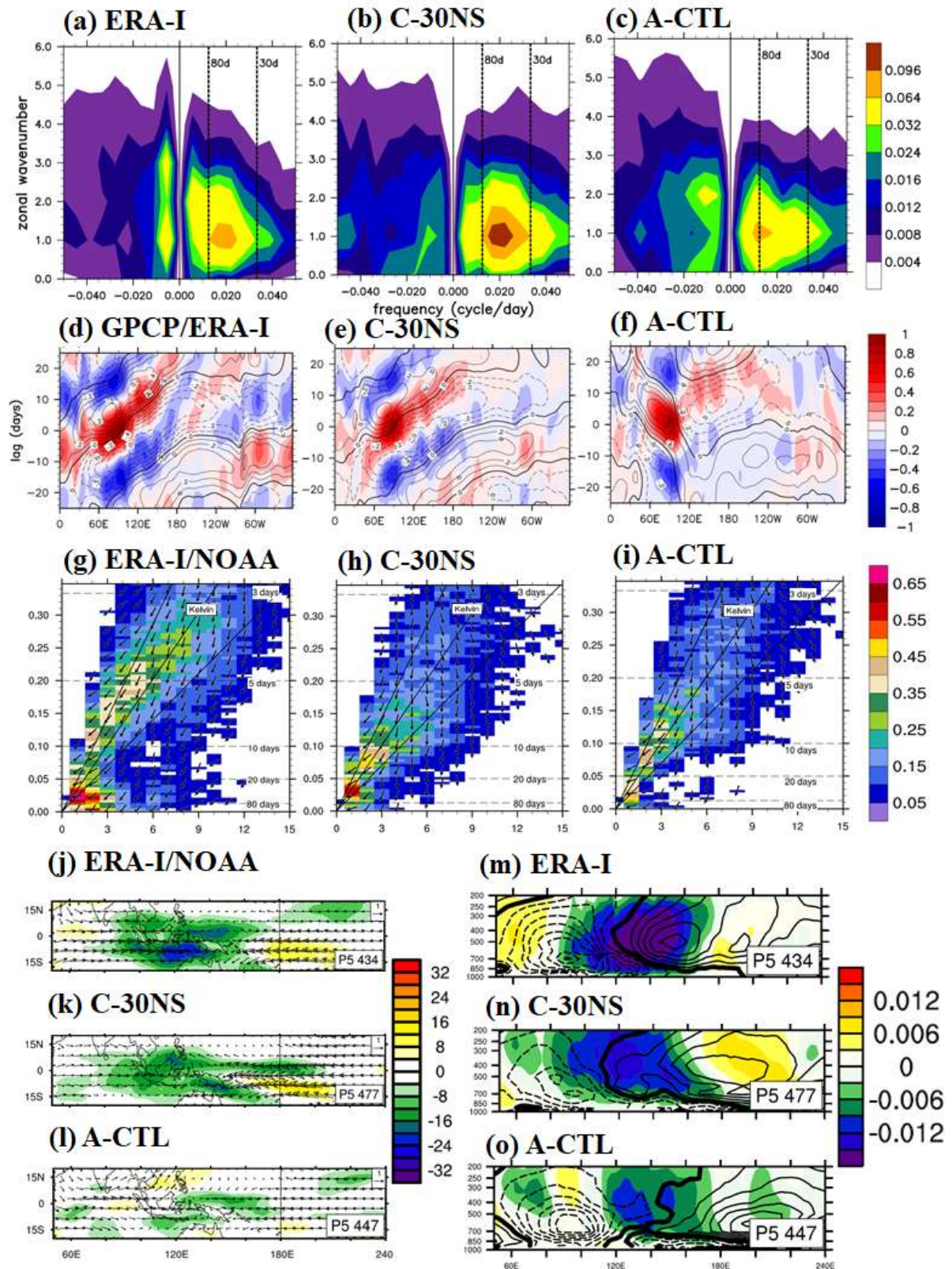
Figure 2. (a)–(c) Zonal wavenumber–frequency spectra for 850-hPa zonal wind averaged
over 10°S–10°N in boreal winter after removing the climatological mean seasonal cycle.
Vertical dashed lines represent periods at 80 and 30 days, respectively. (d)–(f) Hovmöller

diagrams of the correlation between the precipitation averaged over 10°S–5°N, 75–100°E and the intraseasonally filtered precipitation (color) and 850-hPa zonal wind (contour) averaged over 10°N–10°S. (g)–(i) Zonal wavenumber–frequency power spectra of anomalous OLR (colors) and phase lag with U850 (vectors) for the symmetric component of tropical waves, with the vertically upward vector representing a phase lag of 0° with phase lag increasing clockwise. Three dispersion straight lines with increasing slopes represent the equatorial Kelvin waves (derived from the shallow water equations) corresponding to three equivalent depths, 12, 25, and 50 m, respectively. (j)–(l) Composites of 20–100-day filtered OLR (W m^{-2}, shaded) and 850-hPa wind (m s^{-1}, vector) for MJO phase 5 when deep convection is the strongest over the MC and 850 hPa wind, with the reference vector (1 m s^{-1}) shown at the top right of each panel, and (m)– (o) 15°N–15°S averaged p-vertical velocity anomaly (Pa s^{-1}, shaded) and moist static energy anomaly (W m^{-2}, contour, interval 0.003); solid, dashed, and thick-black lines represent positive, negative, and zero values, respectively. The number of days used to generate the composite is shown at the bottom right corner of each panel. (a), (d), (g), (j), and (m) are from ~~observations;~~the ERA-Interim and NOAA post-processed data (abbr. ERA-I/NOAA); (b), (e), (h), (k), and (n) are from the control experiment C–30NS; and (c), (f), (i), (l), and (o) are from the A–CTL.
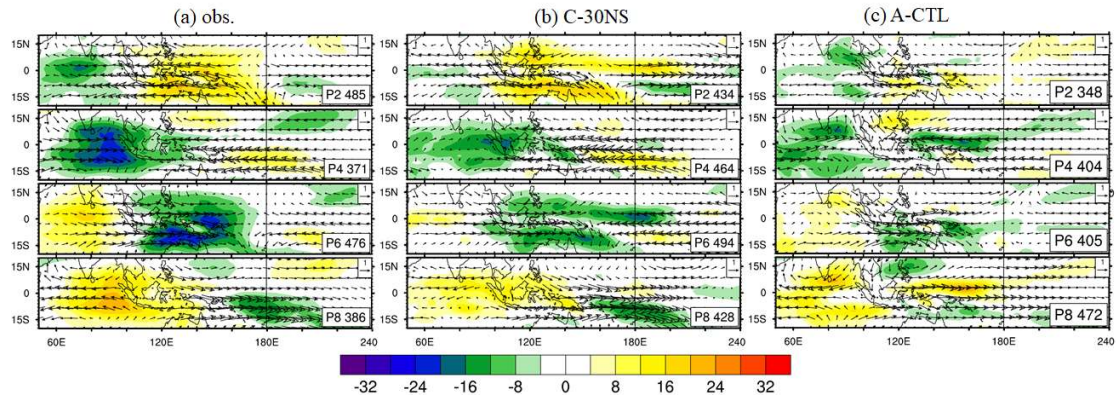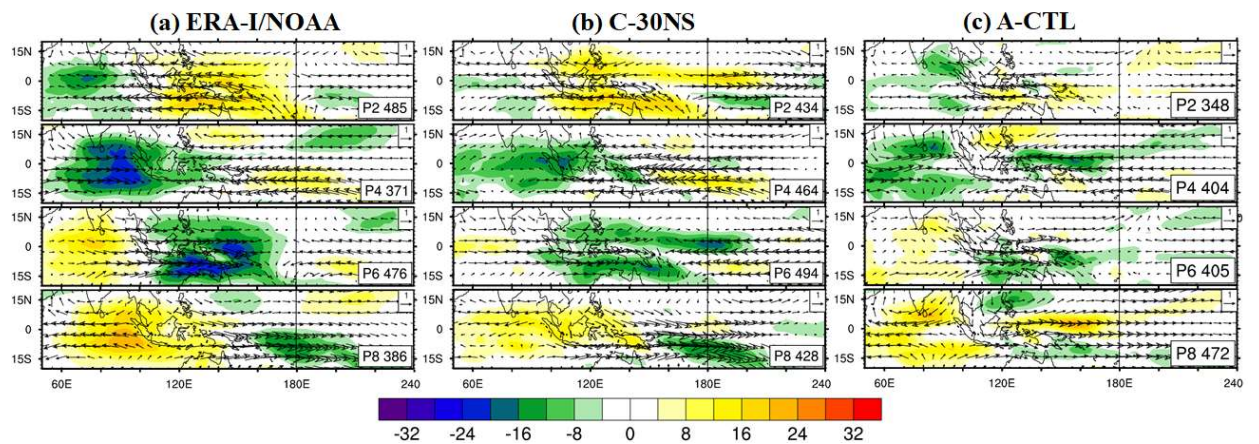
Figure 3. Evolution of the filtered OLR anomaly (W m^{-2}, shaded) and 850-hPa wind (m s^{-1}, vector) at phase 2, 4, 6, and 8: (a) ~~observation~~the ERA-I/NOAA data, (b) the control coupled experiment C–30NS, and (c) the uncoupled experiment A–CTL. The unit of the reference vector shown at the top right corner of each panel is m s^{-1}, and the number of days used for the composite is shown at the bottom right corner of each panel.

1207

66
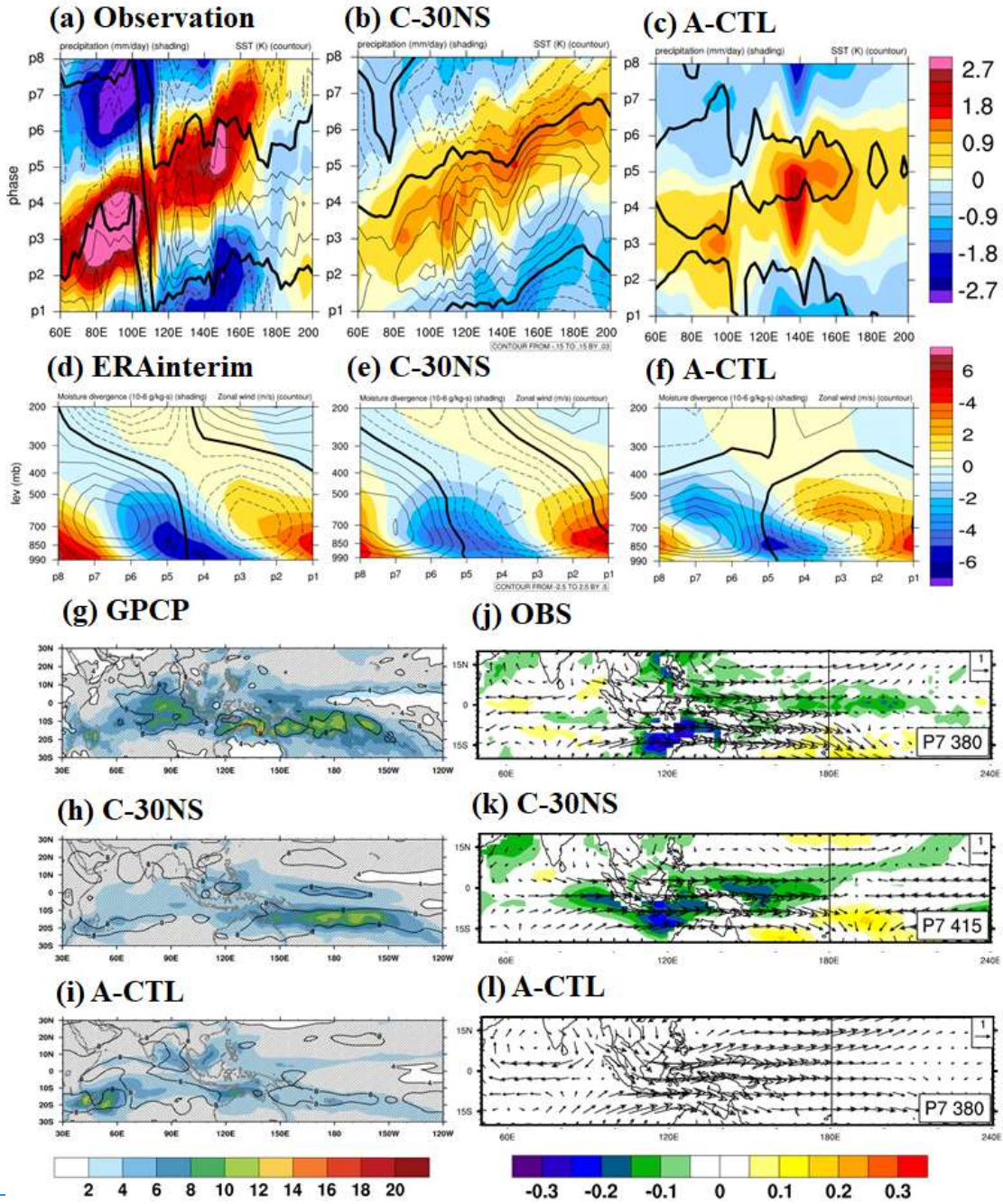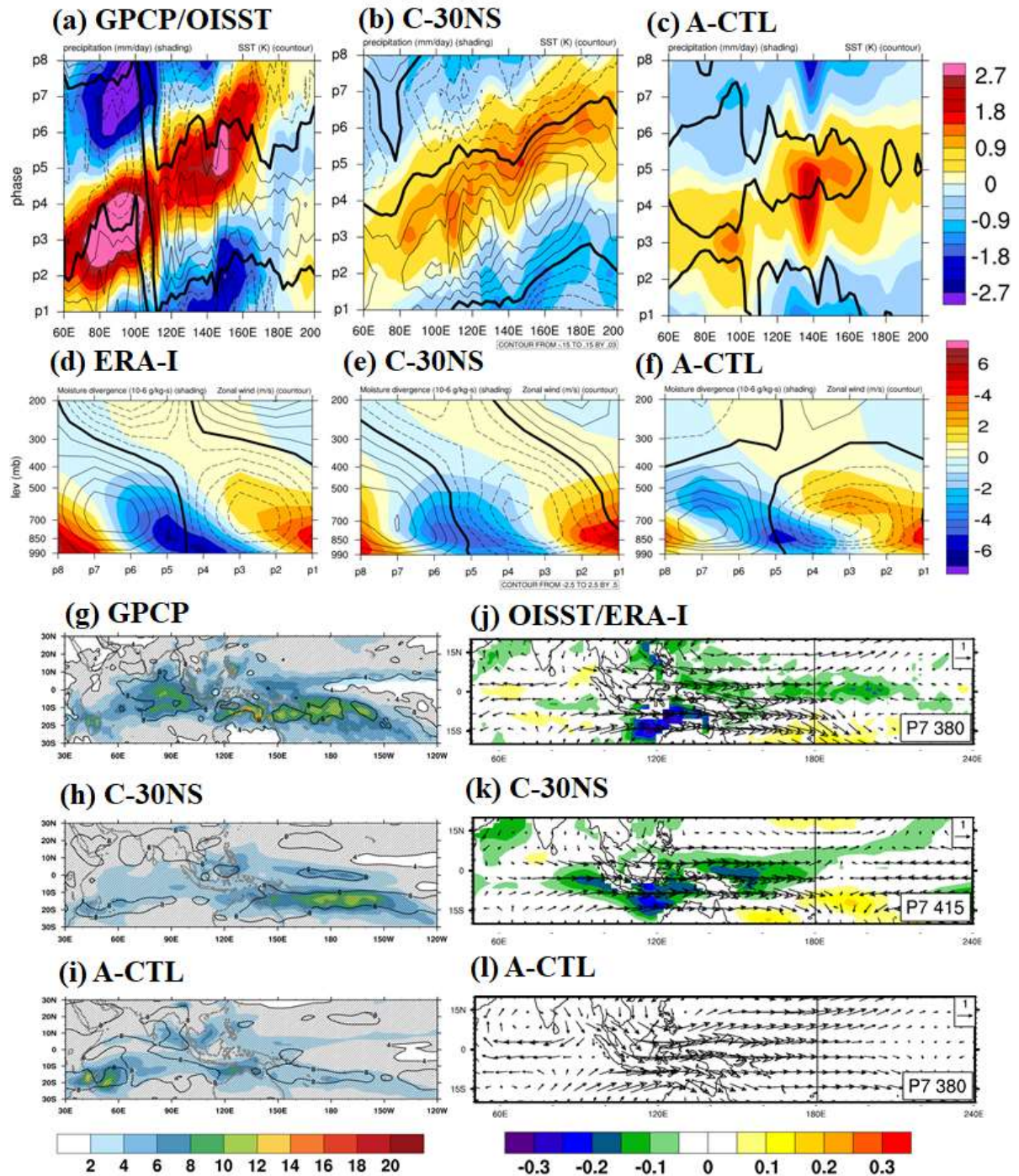
1208

1209

Figure 4. (a)–(c) Phase-longitude Hovmöller diagrams of 20–100-day filtered
precipitation (mm day^{-1}, shaded) and SST anomaly (K, contour) averaged over 10°N–
10°S from phase 1 to 8. Contour interval is 0.03; solid, dashed, and thick-black lines
represent positive, negative, and zero values, respectively. (d)–(f) Phase-vertical
Hovmöller diagrams of 20–100-day moisture divergence (shading, 10^{-6} g kg^{-1} s^{-1}) and
zonal wind (contoured, m s^{-1}) averaged over 10°N–10°S, 120–150°E; solid, dashed, and
thick-black curves are positive, negative, and zero values, respectively. (g)–(i) Variation

1217   of 30–60-day filtered precipitation in the eastern IO and the WP in observation (color

1218   shading), and the ratio between intraseasonal and total variance (contoured) and (j)–(l)

1219   composites 20–100-day filtered SST (K, shaded) and 850-hPa winds (m s^{-1}, vector) at

1220   phase 7 when deep convection was the strongest over the dateline. Reference vector

1221   shown at the top right corner of each panel. (a), (d), (g), and (j) are from the

1222   ~~observation~~ERA-I/NOAA data; (b), (e), (h), and (k) are from the control coupled

1223   experiment C–30NS; and (c), (f), (i), and (l) are from the uncoupled experiment A–CTL.
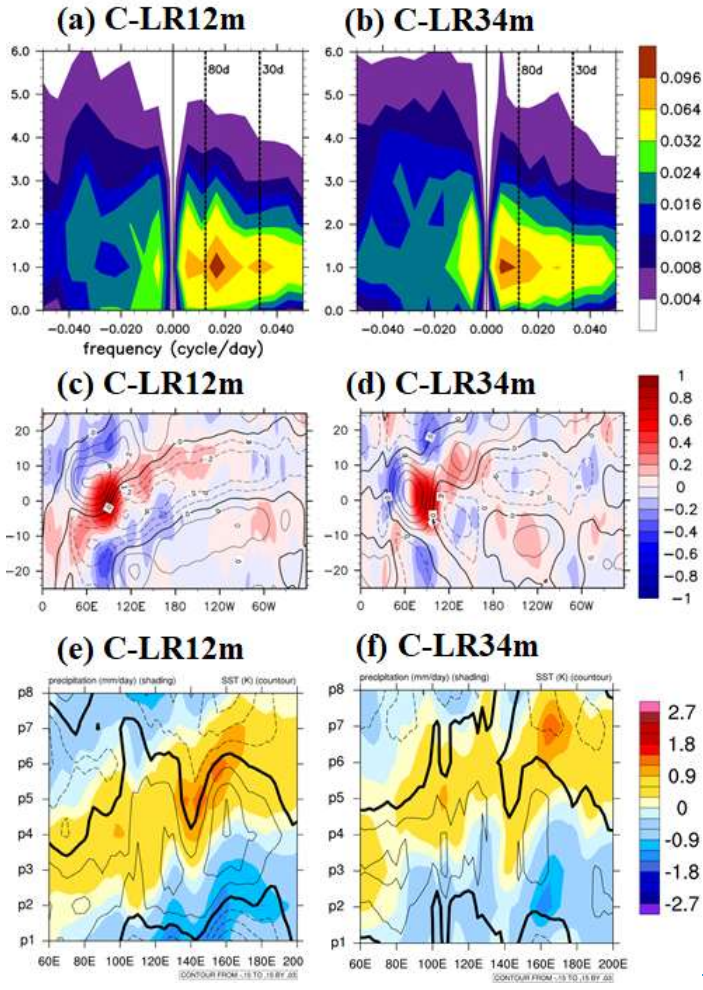
1224
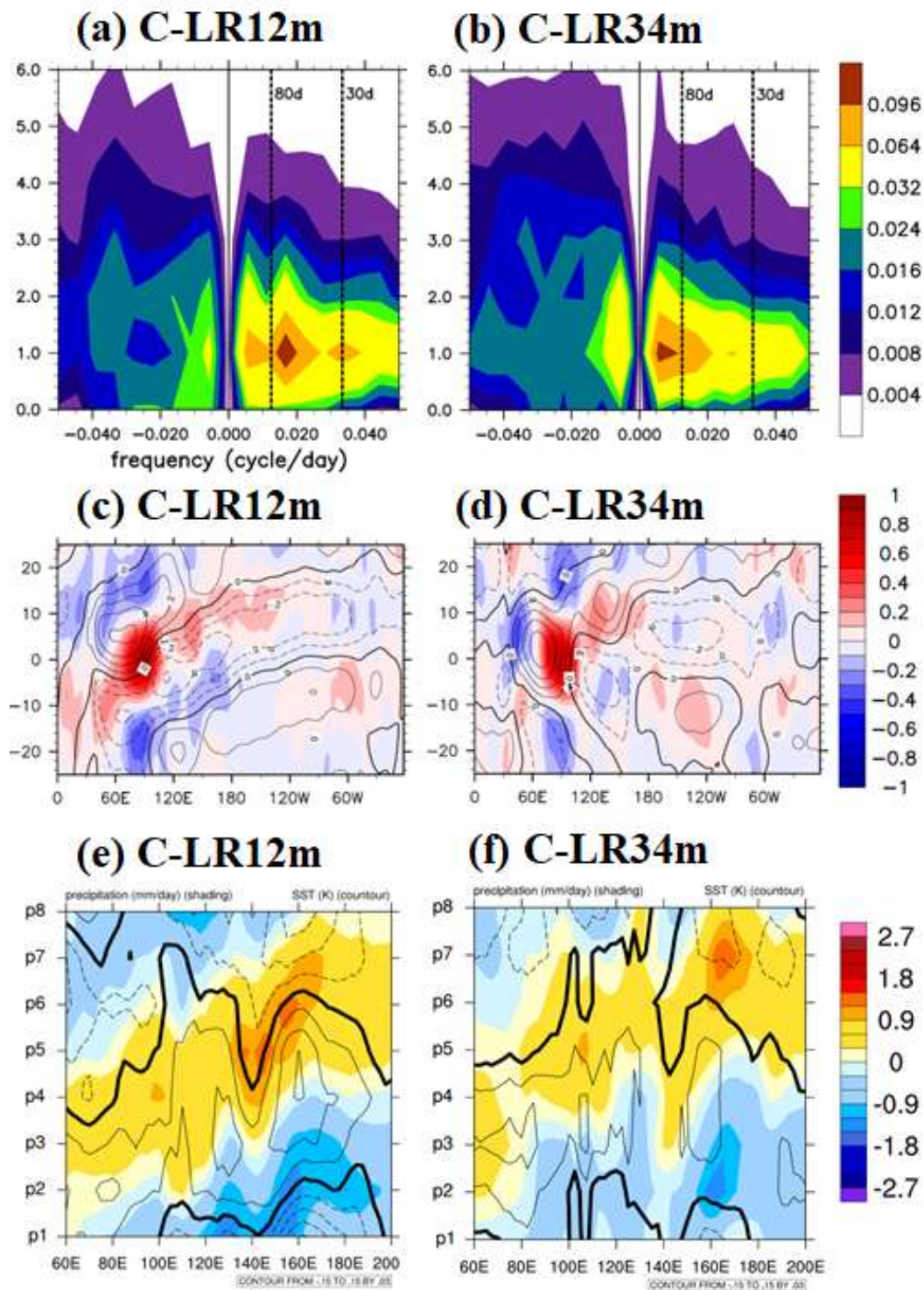
Figure 5. (a)–(b) Same as in Fig. 2(a) but for the C-_LR12m and C-_LR34m. (c)–(d) Same as in Fig. 2(d) but for the C-_LR12m and C-_LR34m. (e)–(f) Same as in Fig. 4(a) but for the C-_LR12m and C-_LR34m.
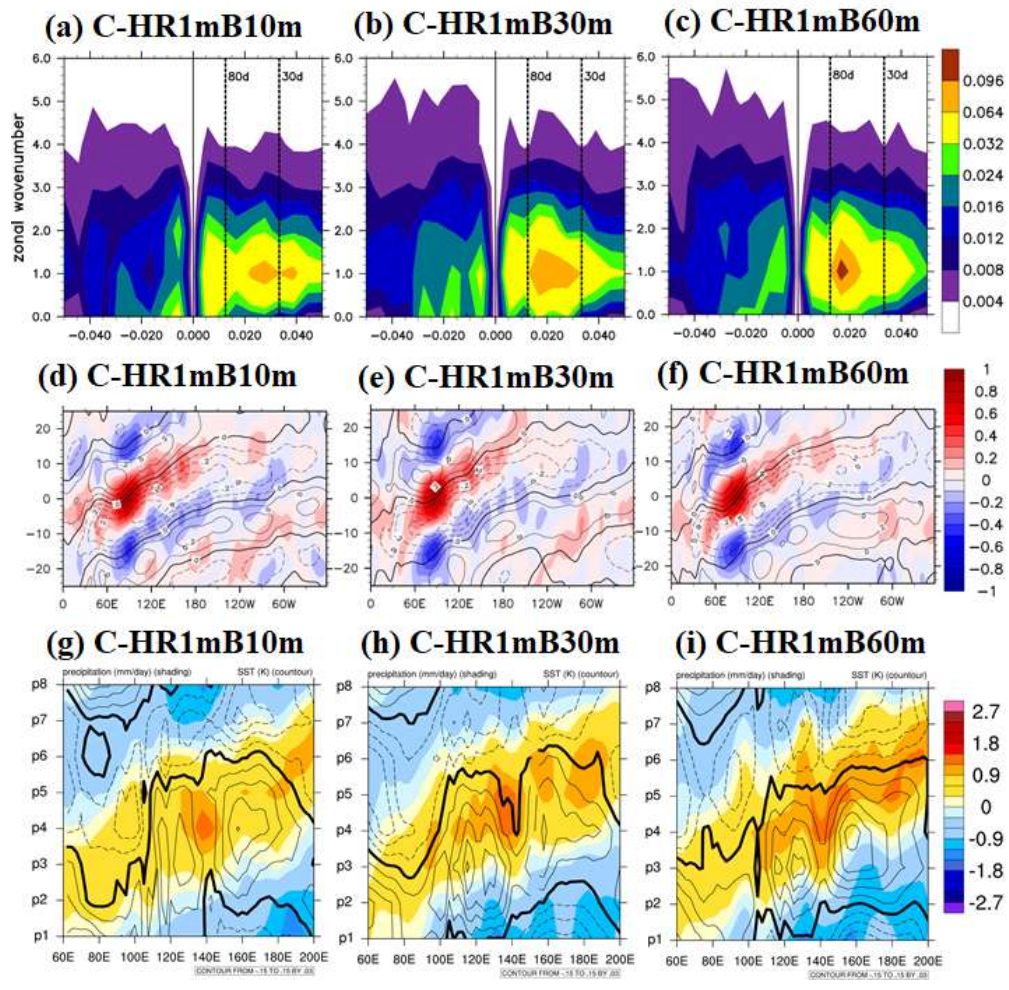
1231
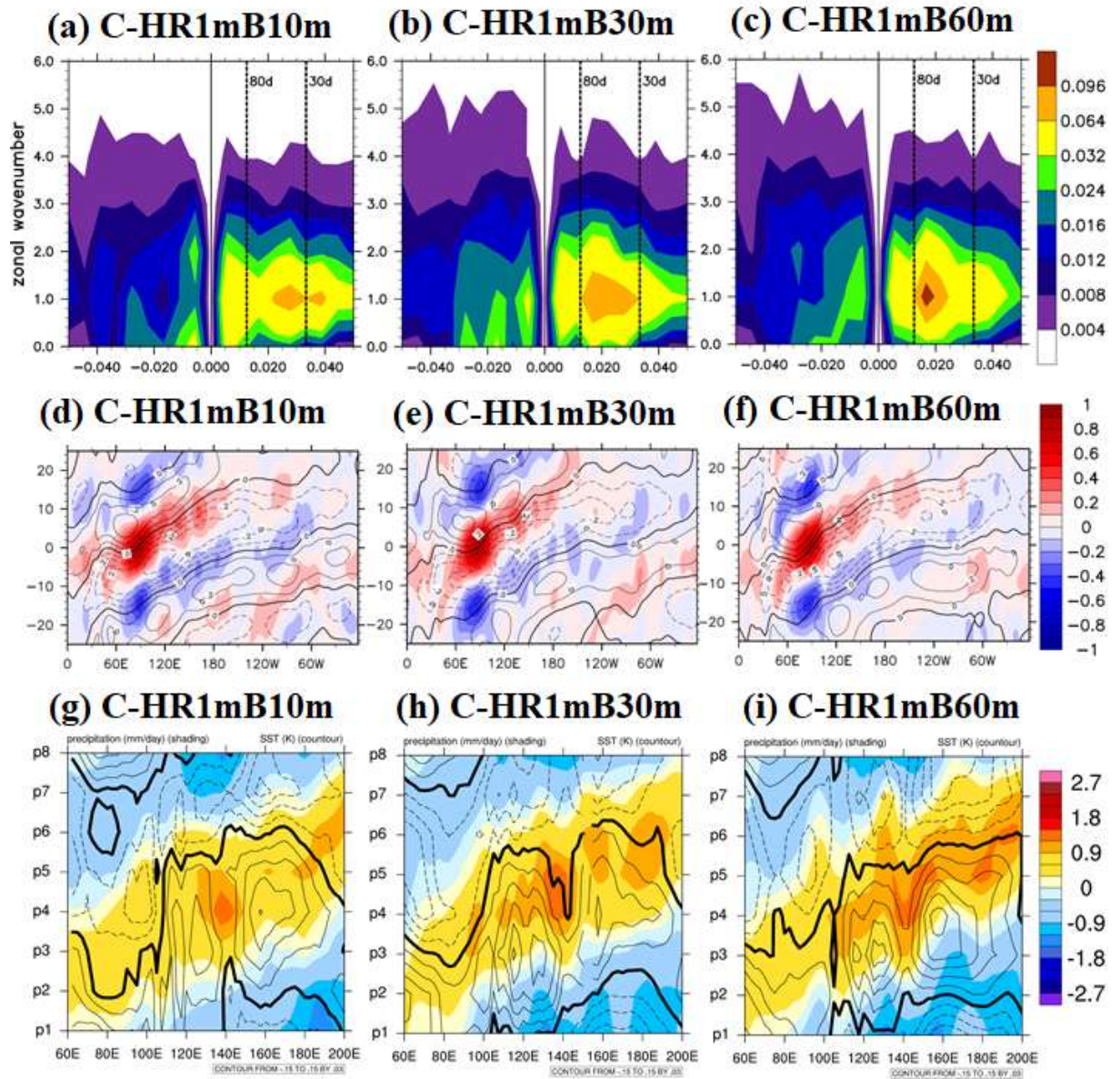
1232

Figure 6. Same as in Fig. 5 but for the C–HR1mB10m, C–HR1mB30m, and C–HR1mB60m.
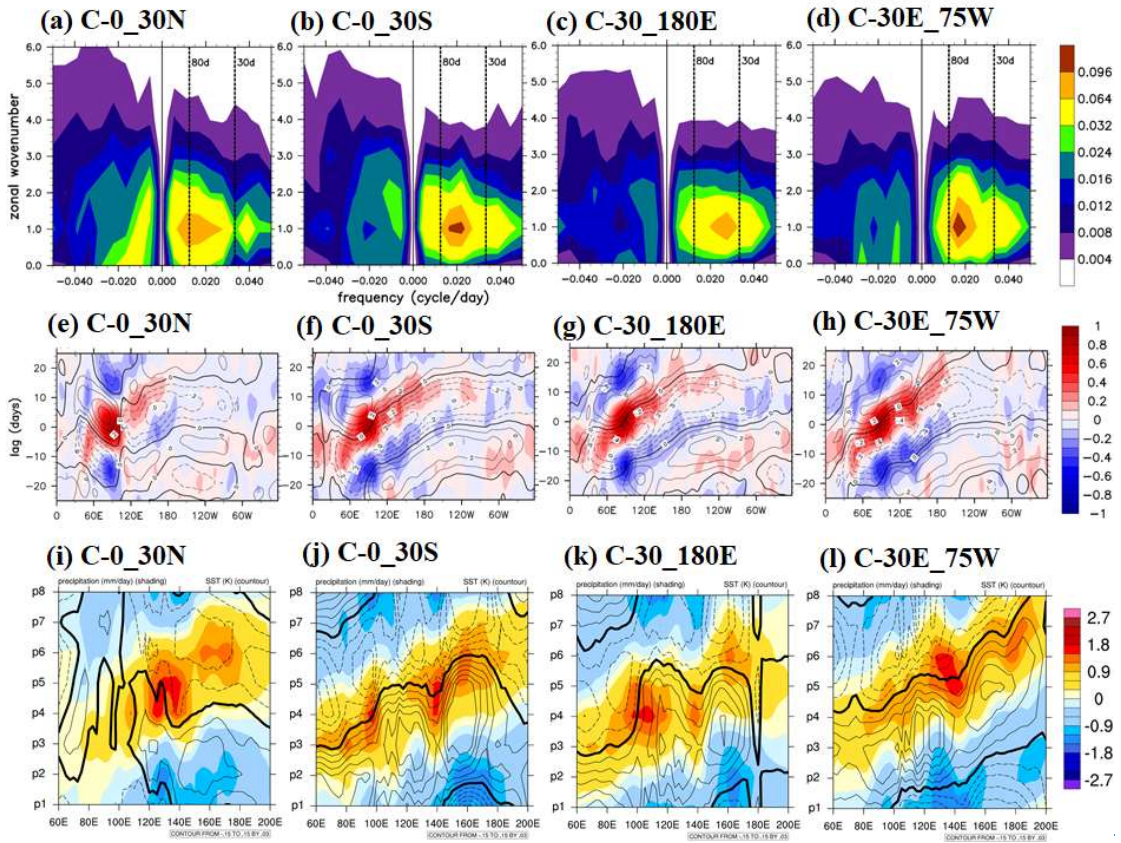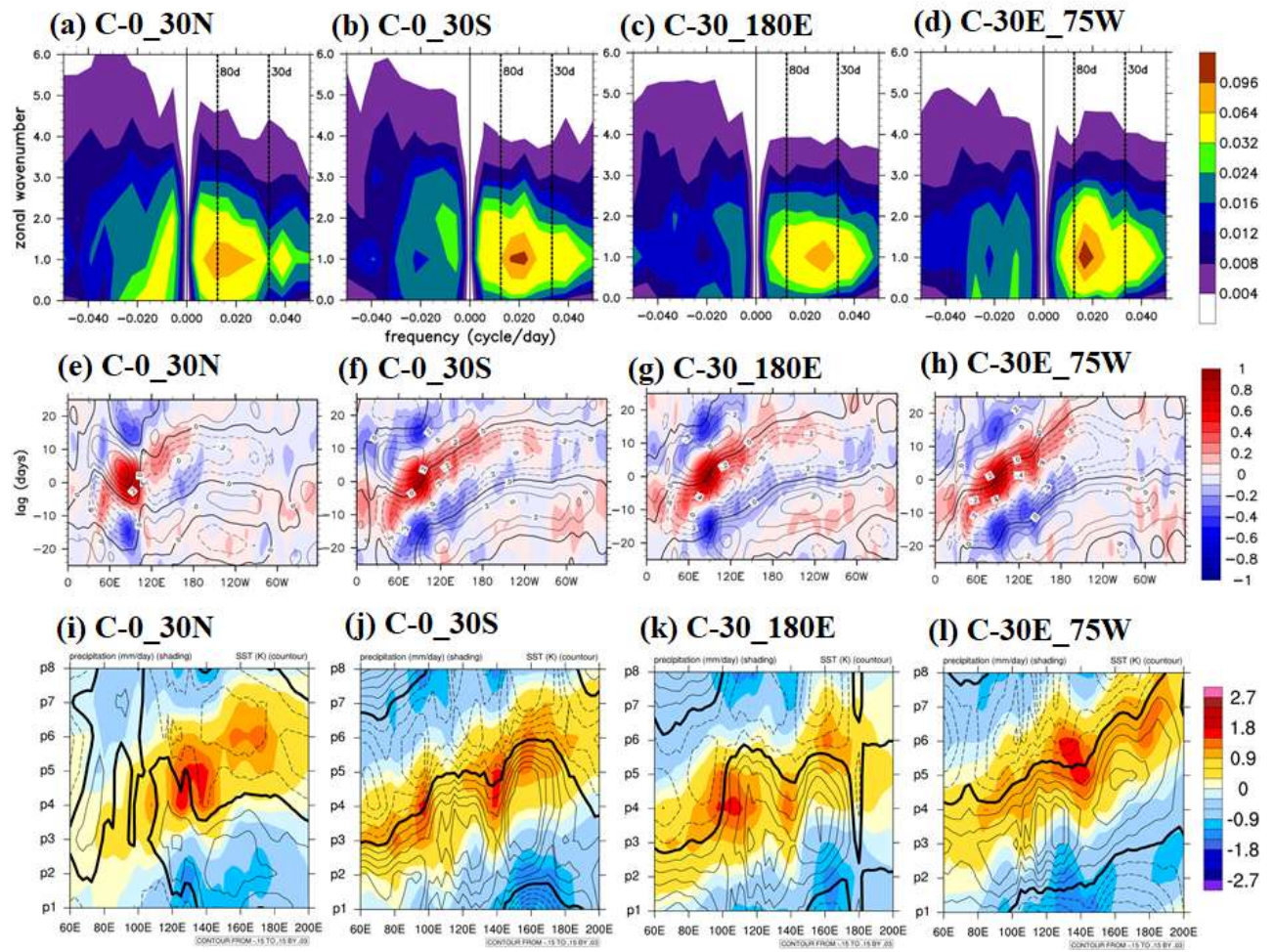
72

1235

73

1236

1237

Figure 7. Same as in Fig. 5 but for the C–0_30N, C–0_30S, C–30_180E, and C–30E_75W.
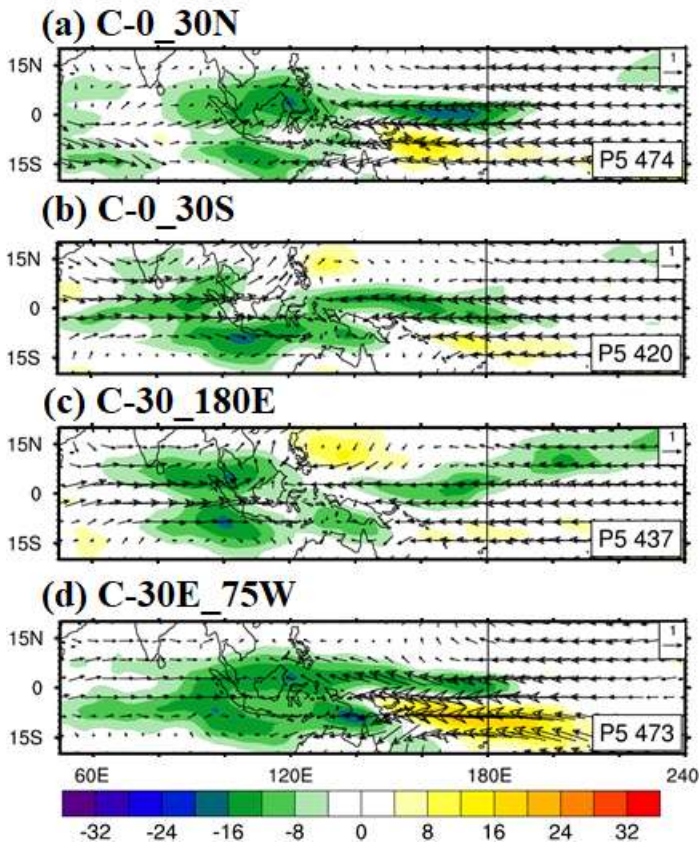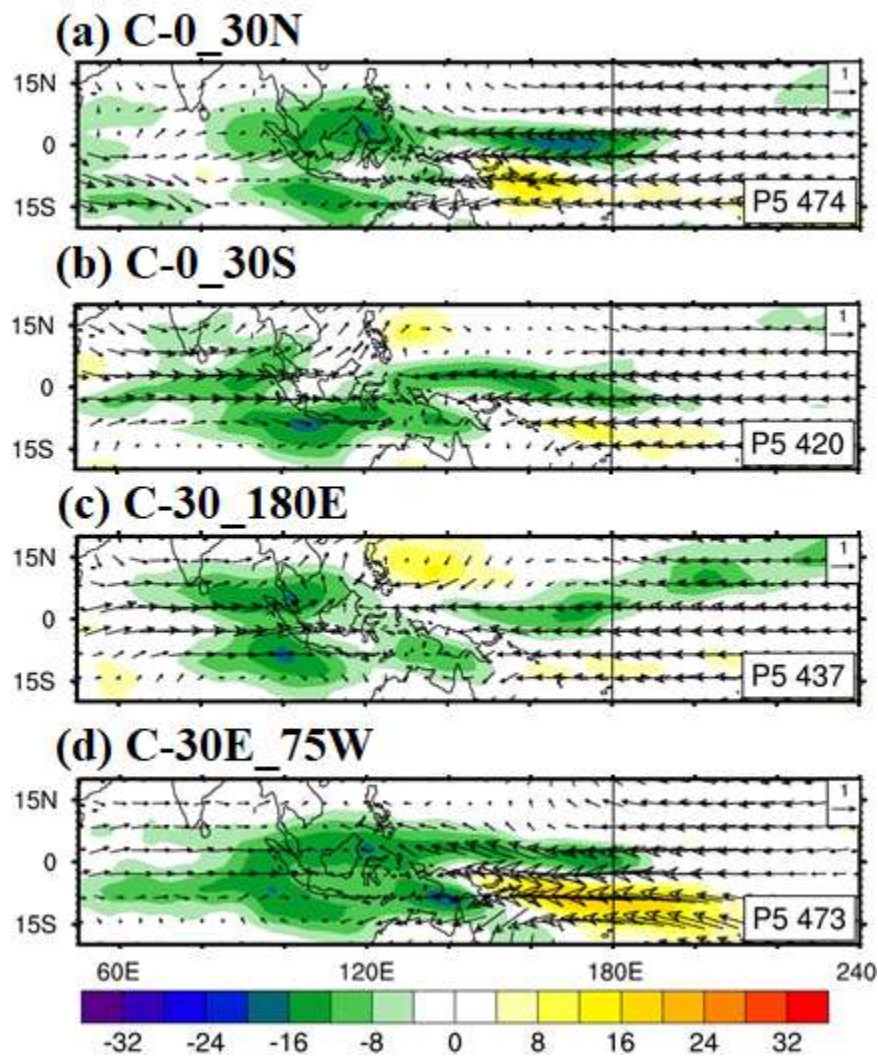
1241

1242

Figure 8. Same as in Fig. 3 but for phase 5 in the C–0_30N, C–0_30S, C–30_180E, and
C–30E_75W.
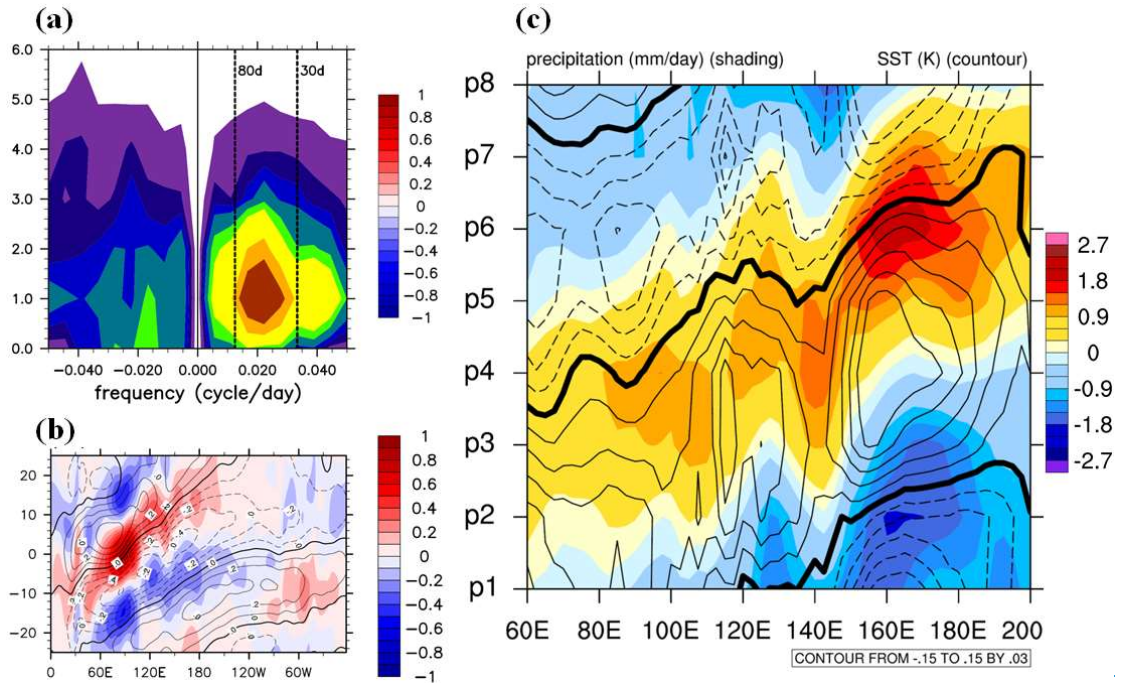
1245
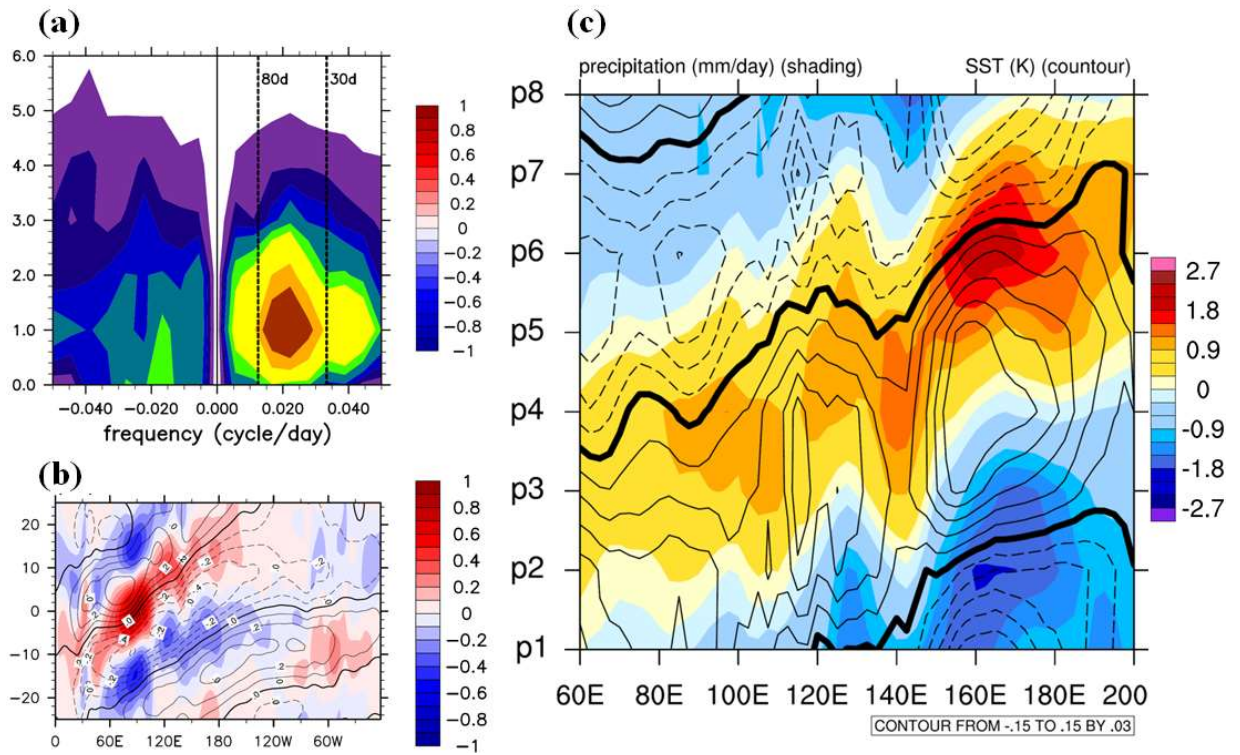
1246

1247

1248 **Figure 9.** Similar as in Fig. 5 but for the C–30NS–nD.
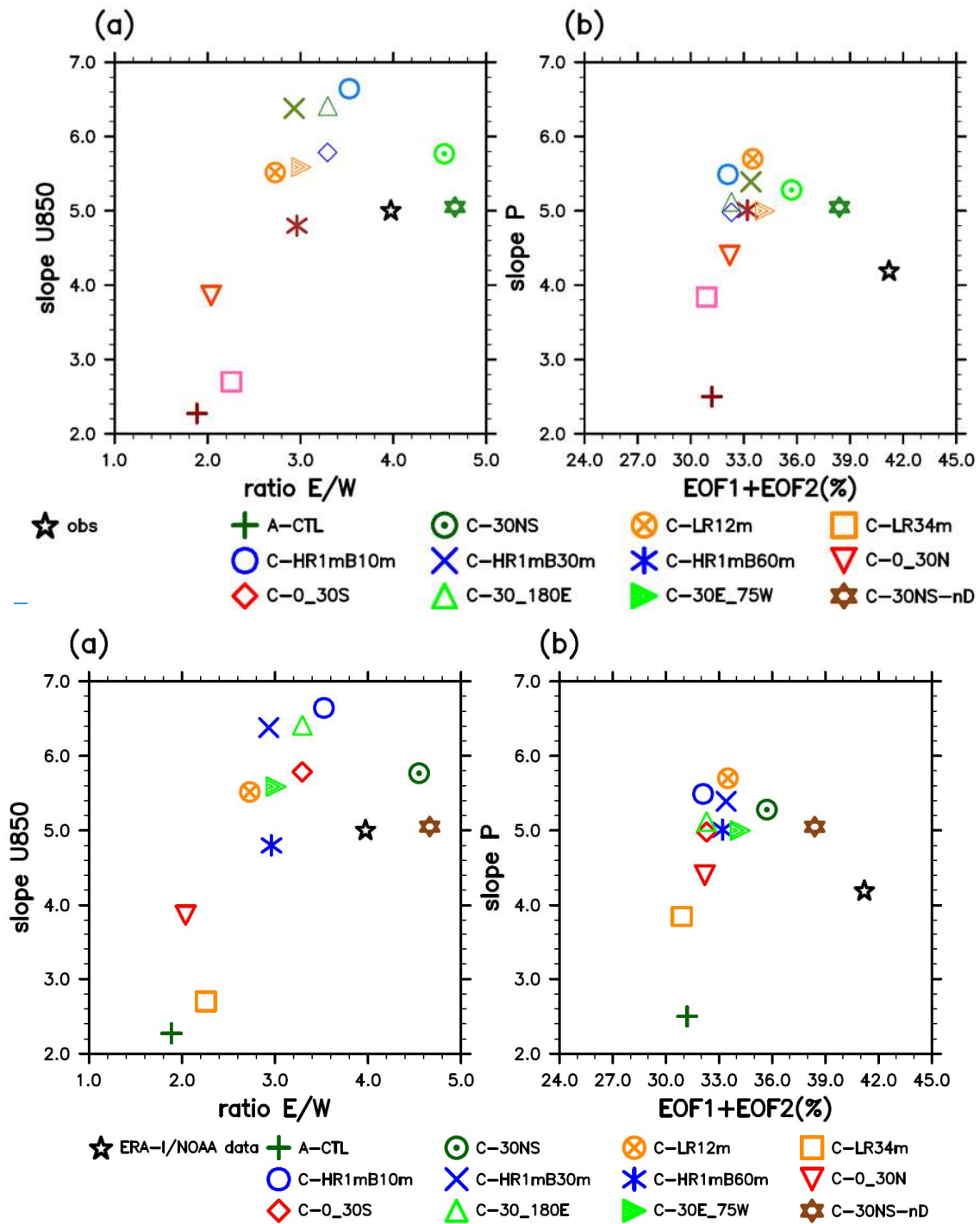
Figure 10. Scattered plots of various MJO indices in ~~observation~~the ERA-I/NOAA data
and 12 experiments: (a) power ratio of east/west propagating waves of wavenumber 1–3
of 850-hPa zonal winds (X-axis) with a 30–80-day period and eastward propagation speed
of U850 anomaly (Y-axis) from the Hovmöller diagram and (b) RMM1 and RMM2
variance and eastward propagation speed of the filtered precipitation anomaly derived
from the Hovmöller diagram.

1 Supplementary Information

Embedding a One-column Ocean Model (SIT 1.06) in the Community Atmosphere Model 5.3 (CAM5.3; CAM5–SIT v1.0) to Improve Madden–Julian Oscillation Simulation in Boreal Winter

8 Yung-Yao Lan, Huang-Hsiung Hsu[*], Wan-Ling Tseng, and Li-Chiang Jiang

10 Research Center for Environmental Changes, Academia Sinica, Taipei 11529, Taiwan

11 [*]*Correspondence to*: Huang-Hsiung Hsu (hhhsu@gate.sinica.edu.tw)
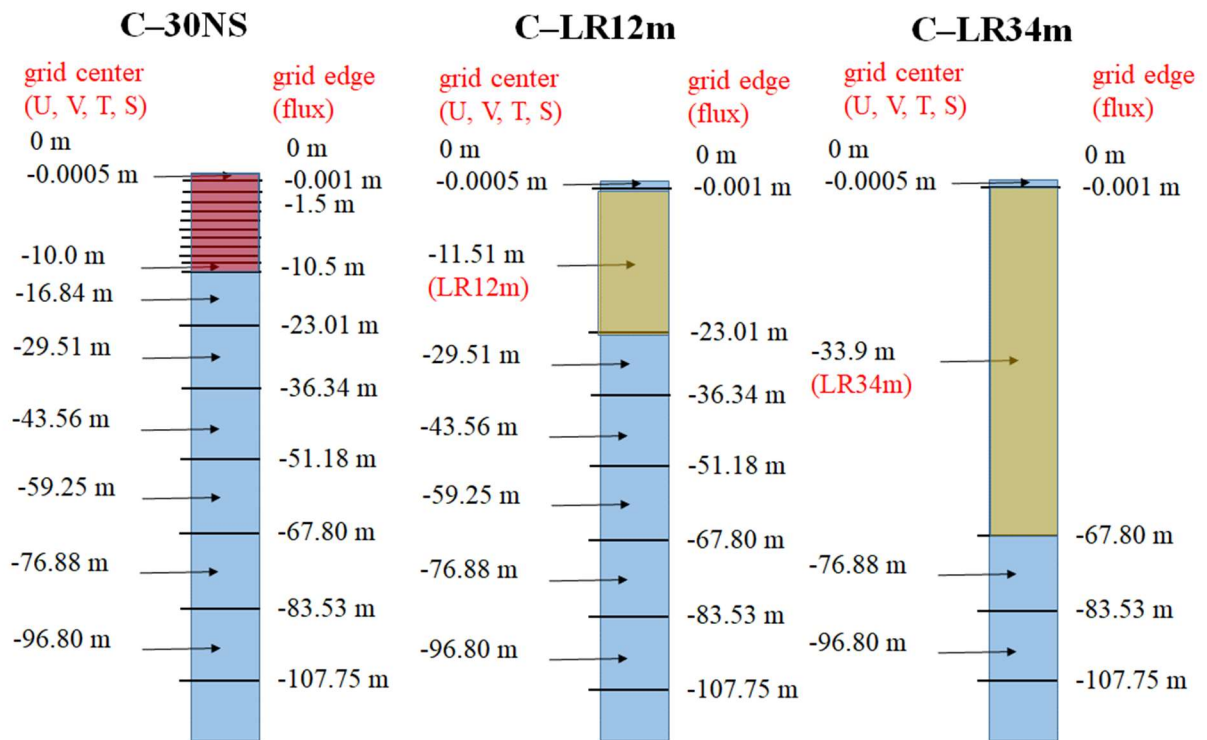
15
16   Figure S1. Diagram showing the vertical grid within 107.8 m in C–30NS, C–LR12m and
17   C–LR34m, the model is as thick as 107.8 meters and with several layers between surface
18   and model bottom. C–LR12m (31 vertical layers) and C–LR34m (28 vertical layers) have
19   a first layer with grid center of 12 m and 34 m, respectively, but have the same vertical
20   discretization as in the control experiment (C–30NS, 41 vertical layers) below the first
21   layer.

24   Figure S2. Diagrams showing the vertical grids in C–HR1mB10m, C–HR1mB30m and

25   C–HR1mB60m. The model bottoms are 10, 30, and 60 m, respectively, unless the seabed

26   is shallower than the above depth.